airestech

400 APPLEWOOD CRESCENT UNIT 100
VAUGHAN, ONTARIO, L4K 0C3, CANADA
1 (855) 725-2034 | WWW.AIRESTECH.COM

American Aires Inc.
Research and Development department

REPORT

R&D: Calculation of the strength and intensity of the electromagnetic field in the interaction of electromagnetic radiation at a frequency of 28 GHz (Wi-Fi 5G) with an Aires 64P1S5G resonator (microprocessor), used in the LIFETUNE Room and LIFETUNE Personal (2020 model)

Project manager:
I. Serov

Researchers:
K. Korshunov
I. Soltovskaya
T. Shamko

Scientific consultants:
Doctor of Technical Sciences, Professor A.V. Kopyltsov of Saint Petersburg Electrotechnical University LETI

Professor of Vilnius Gediminas Technical University, A. Jukna.

2020

TABLE OF CONTENTS

Introduction.
1. Physical model.
2. Mathematical model.
3. Calculation parameters.
4. Algorithm for the calculation.
5. Results and discussion.
Conclusion.
Bibliography.
Appendix 1. Topology of the Aires 64P1S5G resonator (microprocessor).
Appendix 2. Hardware and software.
Appendix 3. Animation.

INTRODUCTION

In connection with the prospect of the use of 5G – new generation mobile networks (6GHz and 28GHz), a fundamentally new microprocessor was developed. It can effectively differentiate the harmful effects of 5G networks' electromagnetic radiation on humans. 28 GHz EM radiation is in the frequency range approved in the USA and Europe for 5G networks.

To simulate the processes occurring in the interaction of Aires resonators (microprocessors), which are manufactured using Micro-Electro-Mechanical Systems (MEMS) technology, with electromagnetic radiation, physical models of such interaction, as well as algorithms and computer programs based on them, were developed.

This software development was necessary, because the various software packages available on the market generally consider interactions in the context of classical physics. However, a number of studies have shown that the processes taking place in this case can only be explained by accounting for the counter wave interaction on the surface of the resonator and the numerous derivative resonances that result from these processes [1-9]. Existing packages do not take these factors into consideration.

The following experiment with the Aires resonator (microprocessor) showed the possibility of using it in a new class of devices used in medicine, energy conservation, and protecting humans from man-made electromagnetic radiation.

This report discusses the interaction of electromagnetic radiation at a frequency of 28 GHz with an Aires resonator (microprocessor) with the 64P1S5G topology (Appendix 1), which is used in the LIFETUNE Room and LIFETUNE Personal (2020 model). The calculations were made on hardware using software (Appendix 2).

In order to most closely approximate specific technical problems: the design of the simulated element, the range of electromagnetic radiation corresponding to the frequency of a Wi-Fi 5G router (28 GHz) and other modern mobile communication devices, the following physical model was considered in the simulation.

1. PHYSICAL MODEL

Aires resonators (microprocessors) are self-affine circular diffraction gratings with a fractalization factor of 2 and the number of fractalization axes corresponding to the number of the topological scheme (from 8 to 64).

Characteristics of the Aires 64P1S5G microprocessor

- Number of fractalization axes: 64
- 1 level of fractalization + protopype:

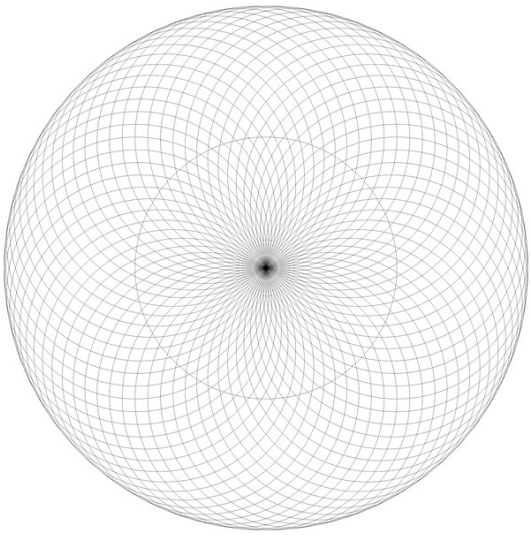

Fig. 1. Topology of the Aires 64P1S5G resonator (microprocessor), which is a flat cut through the center of the self-affine hypersphere. Prototype, diameter $D_1 = 9.696*10^{-3}$ m, number of objects $N_0 = 65$, density $P_0 = 0.88$ (1/m^2)

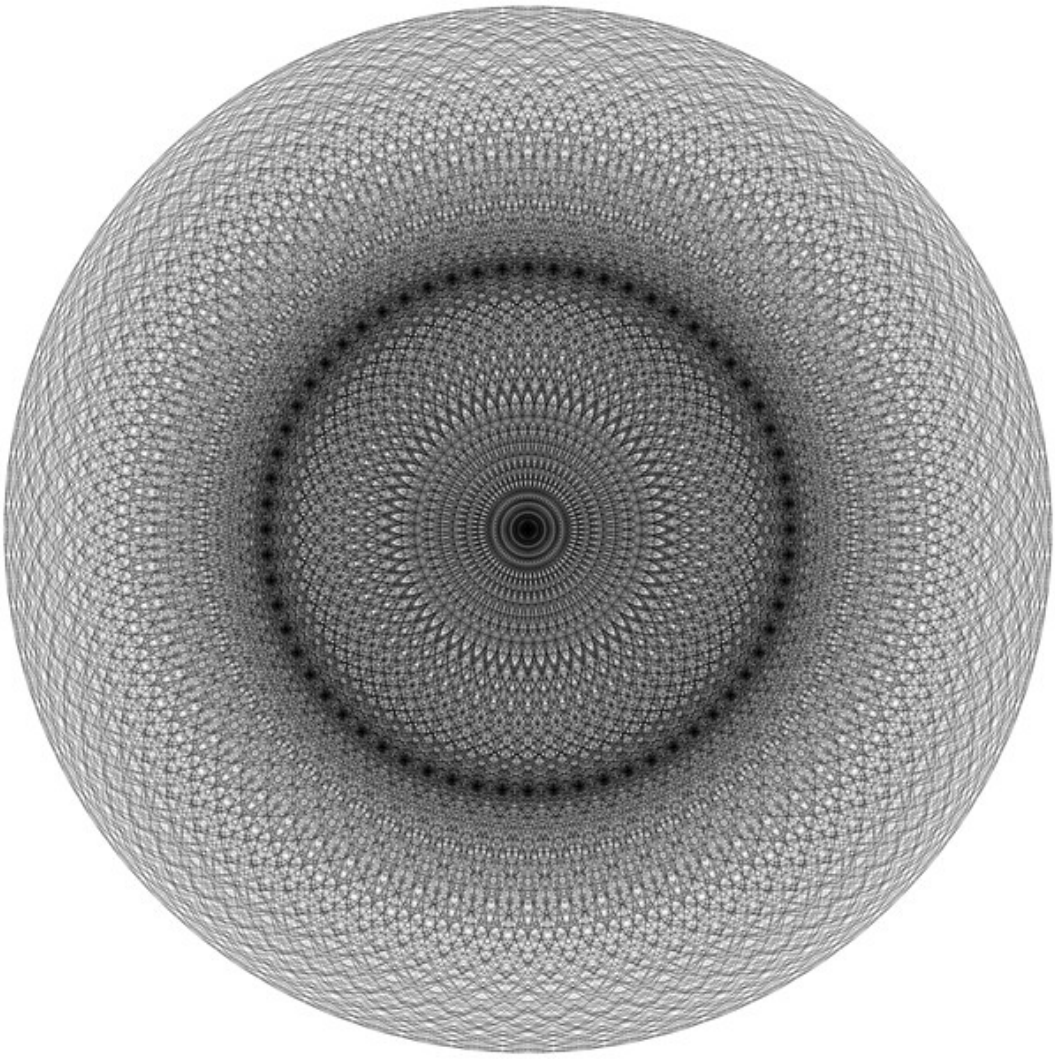

Fig. 2. Aires 64P1S5G resonator (microprocessor) topology,
*derivative 1, diameter D_2 =19.4*10^{-3} m,*
number of objects N_1 = 4161, density P_1 = 14 (1/m^2)

Since the total topology density is divided into several zones, in this case we calculate the average density per unit area (m^2). The field reflex from each zone will be distinguished by the field density corresponding to that zone.

- Number of rings (slit resonators): 4161
- Slit parameters (width / height): $0.2*10^{-6}$ m / $0.8*10^{-6}$ m.

The radial axes of fractalization are arranged in pairs strictly by the diameters of the circuit, thereby forming a counter resonant interaction corresponding to the formula (1), which describes the equilibrium principle of a hypercomplex interaction system based on the deepest spatial-temporal amplitude-frequency harmonization of wave fronts, which correlates with the stationary Schrödinger equation for a quantum system (superposition principle), which defines the

arising wave function as a vector sum of all wave functions of elements of the system.

The phenomenon occurs in the case of wave interactions of opposite functions, when the agents participating in the interaction are maximally harmonized among themselves in terms of amplitudes, frequencies, phases (focal point of the system) and the spatial interaction diagram.

This process makes it possible to locally accumulate, register, and use the highest potential.

When presenting the base unit of the system as B_0 (x_1, x_2, ..., x_n), and the functions of the fractal mapping (for example, scaling and shifting) through $F(B_0)$, the iterative process of the formation of the fractal structure, which reflects the hierarchical principle of the symmetry of the structural organization of the counter interaction system, can generally be described as:

$$F_k(B_0) = \sum_{i=1}^{k-1} F_i(B_0)$$

.

The level of contradictions within any arbitrarily taken hypercomplex system, if obtaining a functionally active and maximally stable design is required, should tend to zero, defining the principle of universal multi-level coordination (coherence).

The statement applies to both a three-dimensional "X, Y, Z" system, and to a self-affine hyperspherical form that has an infinite number of structural components of different dimensionality that tend to absolute symmetry, according to Noether's theorem.

$$\sum_{i=1}^{n} \frac{\partial \mathrm{L}}{\partial \dot{\mathrm{x}}_i} \delta_i = constant$$

For the case of the reciprocal vector interaction, the equation can be written as:

$$X^n + Y^n + Z^n + \ldots + N^n \rightarrow 0$$

This expression implies the simultaneous solution of all equations comprising the given spatial hypercomplex. The number of these equations is equal to the number of interactions that define the process under consideration.

In the case of interaction of system-wide hyper-objects of different fractal

dimensions with respect to a common "zero" center (a phase transition to the next quantum fractalization zone), the equation takes the form:

$$\sum_{k=1}^{n} X^k + \sum_{k=1}^{n} Y^k + \sum_{k=1}^{n} Z^k + \cdots + \sum_{k=1}^{n} N^k \to 0 \qquad (1),$$

where 0 is the focal point (center point) of the circuit, which is a singularity zone where the potential density tends to infinity and its amplitude approaches zero.

The resonators' topological circuits have the properties of the self-affine analogs of fractal antennas [4-8]. A fractal antenna is an antenna whose active part has the form of a self-similar curve or any other figure similarly divided or consisting of similar segments.

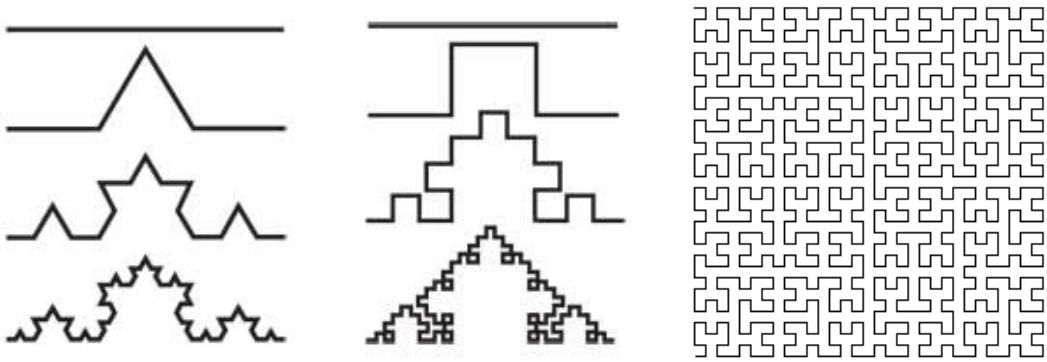

Fig. 3. Emitters based on Koch and Peano fractals

It should be noted that any system that adheres to the same principle for forming constituent elements, for example, the Fibonacci series, will also be a fractal object, i.e. will have the properties of self-similarity and scale invariance.

Typically, almost all biological objects widely represented in nature tend to form corresponding fractal structures by multiplying the self-similar structural elements (Fig. 4) that form their basis.

Fig. 4. Fractals in nature

This is due to the need to interact with the widest possible range of electromagnetic radiation frequencies in the environment for the purpose of accumulating the energy-information potential necessary for the vitality of any biological organism (metabolism and homeostasis processes) and adequately systematized reversal of genetic programs in the process of its synthesis. An analogous process associated with the presence of the required level of harmonized energy potential is also observed in inanimate nature in the formation of the structures of any crystal lattices (Figures 5, 6).

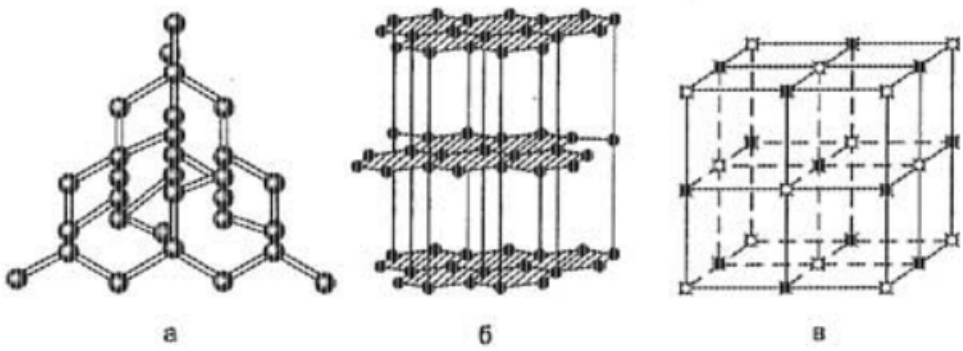

Fig. 5. Crystal lattices: a) diamond, b) graphite, c) rock salt

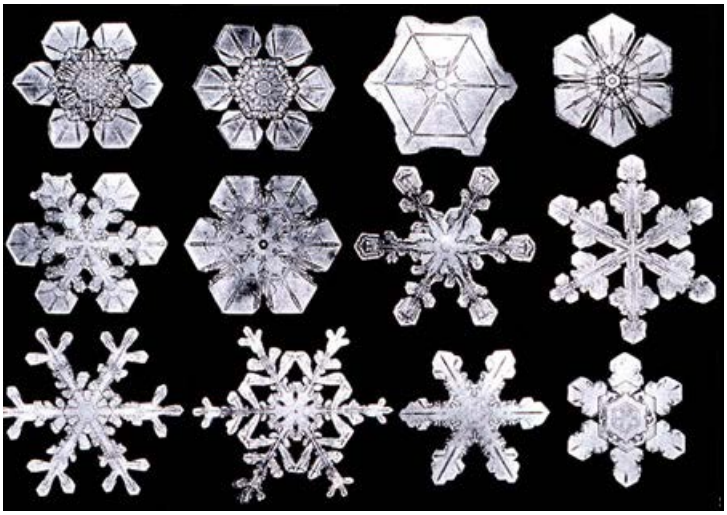

Fig. 6. Photographs of ice crystals

The specific properties of the Aires resonator (microprocessor) as a fractal ring diffraction grating are broadband interaction with external electromagnetic radiation and a high degree of signal amplification due to the summation of currents and the resulting iterative resonance effect as an integral superposition of subresonant processes. Thus, the resonator may be considered an analog of a fractal antenna.

The total length of the rings forming the resonator's self-affine matrix as a conductor is composed of the sums of circumferences that form its topological circuit and determines the lower boundary of the frequency range of the resonator's interaction with incident electromagnetic radiation (Table 1).

Table 1.

Microprocessor model	**64P1S5G**
Ring diameter	$4.848*10^{-3}$ m
Number of rings	4161
Length of the conductor (antenna)	63.37 m
Lower threshold of interaction frequency	$2.37*10^{6}$ Hz

Because the Gabor-Denisyuk hologram theory says that any wave superposition has the same properties as the regular system that generated it, we can consider the wave superposition (hologram) arising from the material regular circuit (Fig. 2) as the first derivative, which has the corresponding properties of the base grating that gave rise to it.

In turn, the first derivative, which is a regular system of maxima and minima of the field strength, acts as a secondary diffraction grating and, by interacting with the radiation incident on the system, forms the next level of a

similar wave superposition, which can be called the second derivative. In the same way, the system of maxima and minima of the field strength of the second derivative generates a new superposition or a third derivative, which always represents deep interference, i.e. it includes the interaction of waves, half-waves, and quarter-waves, thus forming a three-level system of resonant interconnections.

In the end, the result of this process as the fourth derivative is the process of harmonizing the different types of external radiation through the structure of the second derivative giving rise to this process (superposition from a regular fractal base), which in this case acts as a universal filter initiating a direct and inverse Fourier transform. Thus, there is a differentiation of the initial wave flow (28 GHz) into eigen harmonics with the subsequent formation of a matrix of electromagnetic superpositions that is spatially-temporally harmonized with respect to the amplitudes and frequencies.

The Aires resonator (microprocessor) is a type-n monocrystalline silicon substrate with a crystallographic plane of 100 (Miller index), with dimensions of $19.6*10^{-3}$ m x $19.6*10^{-3}$ m and a thickness of $0.5*10^{-3}$ m, whose surface has an absolutely symmetric fractal system of annular slits with a rectangular cross section with a width of $0.2*10^{-6}$ m and depth $0.8*10^{-6}$ m, forming a regular self-affine structure that obeys the laws of self-similarity and scale invariance (Appendix 1).

The incident radiation's interaction with the silicon substrate produces polarization and a surface wave.

According to modern scientific knowledge, everything is electromagnetic in nature. A material's crystal lattice is a certain ordered, periodic field structure. Erwin Schrödinger, an Austrian Nobel laureate and one of the founders of quantum physics, was the first to express this idea. In turn, any material structure creates a periodic electromagnetic field (superposition) and is maintained by this same field. Moreover, the perfect structures initiate a maximally coherent response that is strictly systematized in terms of amplitudes, frequencies, phases, and the interaction diagram.

Hence we can draw the following conclusion: since the silicon substrate has an appropriate crystal lattice whose domains can be regarded as a regular system of conductors representing a fractal complex, the total length of such domains will determine the wavelength and the frequency range of the object's response to external electromagnetic radiation. Of course, this phenomenon requires additional research.

When the resonator interacts with the radiation incident on its surface, a

surface wave appears and is reflected from the surface with absorption in the slits, which leads to a redistribution of the characteristics of the electromagnetic field. The resonator's slit structure can be considered as a regular topology of the surface of a self-affine silicon wafer (substrate). Both the distribution of the electric field strength above the resonator surface and the distribution of the field's energy flux density (intensity) were modeled.

2. MATHEMATICAL MODEL

In the modeling, it is assumed that the charge carriers are concentrated in the slits. Thus, the potential density and, accordingly, the calculated intensity within the slit will depend on its geometry. In our case, since the slit width $b = 0.2*10^{-6}$ m and the slit depth $glu = 0.8*10^{-6}$ m, when an electromagnetic wave passes through the resonator surface during interaction with a slit, we consider two variants of wave propagation: movement over the slit (path l_1) and motion along the slit (path l_2):

$$l_1 = b = 0.2 * 10^{-6} \ (m),$$

$$l_2 = b + 2 * glu = 9b = 9 * 0.2*10^{-6} = 1.8*10^{-6} \ (m).$$

Thus, the path difference is:

$$\Delta l = l_2 - l_1 = 9b - b = 8b = 8 * 0.2*10^{-6} = 1.6*10^{-6} \ (m).$$

If the initial strength on the surface of the resonator has a gain of 1, then it can reach a maximum of 8 in the slits. To calculate the strength, a gain coefficient $K_l = 2 \div 8$ depending on the density of the resonator's topological circuit, i.e. in low density areas of the circuit $K_l = 2$, in high density zones $K_l = 8$.

$$E_0` = E_0 * K_l ,$$

where E_0 is the initial (background) electric field strength, $E_0`$ is the electric field strength, including the gain.

To describe the current calculation model, it is assumed that the source radiation falls on the AIRES resonator (microprocessor) uniformly from all sides. Thus, we have a radiation source in the form of a hemisphere with radius *R,* which is significantly greater than the diameter of the resonator.

The radiation is distributed along the DCA trajectory (Fig. 7). Point D is on the sphere with radius *R*. Point C is on the resonator wafer. Point A is on the receiver (the space above the resonator wafer), and the strength of electric field *E* is determined at this point. Point C has 2 possible locations – in the slit and on the surface of the resonator. If point C is on the surface, then the incident radiation at point C is reflected (the angle of incidence is equal to the angle of reflection). If point C is in the slit, then the incident radiation at point is absorbed.

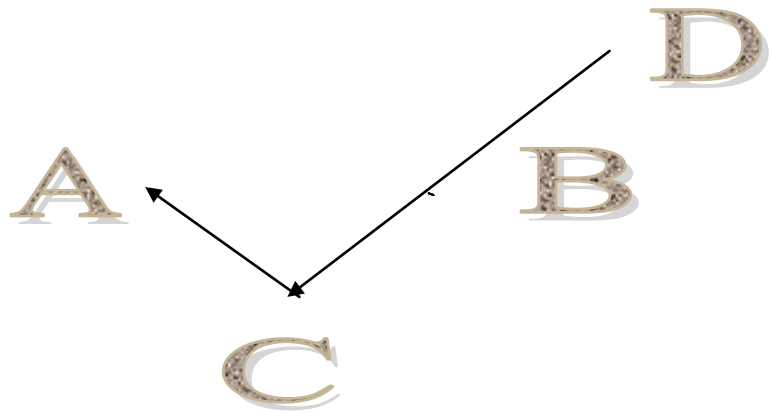

Fig. 7. Trajectory of the incident radiation DCA.

The smooth surface of the resonator is broken into square cells with side h and point C successively (in a cycle) traverses every node in this two-dimensional grating. The receiver is the three-dimensional space around the resonator, divided into cubic cells with side h and point A successively (in a cycle) traverses every node in this three-dimensional grating. At each time t , the coordinates of points A (on the receiver) and C (on the resonator) are assumed to be known.

We assume that we know the intensity of the incident radiation E_0 and the frequency of the radiation ω at point D (radiation source).

We need to find: the strength of electric field E at point A (receiver).

If the coordinates of points A (x_A, y_A, z_A) and C (x_C, y_C, z_C) are known, then the coordinates of point B (x_B, y_B, z_B) can be determined using the following formulas:

$$x_B=2\,x_C-x_A$$
$$y_B=2\,y_C-y_A$$
$$z_B=z_A$$

Point B is symmetric to point A in the DCA plane relative to the normal to the resonator's surface at point C.

Equation for the line segment BC:

$$\frac{x-x_C}{x_B-x_C}=\frac{y-y_C}{y_B-y_C}=\frac{z-z_C}{z_B-z_C}$$

Equation for the line segment AC:

$$\frac{x-x_C}{x_A-x_C}=\frac{y-y_C}{y_A-y_C}=\frac{z-z_C}{z_A-z_C}$$

Distance between points A and C:

$$L1=\sqrt{(x_A-x_C)^2+(y_A-y_C)^2+(z_A-z_C)^2}$$

Coordinates of vector CA:

$$x_{CA}=x_A-x_C$$
$$y_{CA}=y_A-y_C$$
$$z_{CA}=z_A-z_C$$

Direction cosines of vector CA

$$cos(CA_x)=x_{CA}/L1$$
$$cos(CA_y)=y_{CA}/L1$$
$$cos(CA_z)=z_{CA}/L1$$

Equation for sphere with radius R with center at (x_0, y_0, z_0) (coordinates of the center of the resonator):

$$(x-x_0)^2+(y-y_0)^2+(z-z_0)^2=R^2$$

The coordinates of point D (x_D, y_D, z_D), the intersection of line segment BC and the sphere with radius R, are determined from the following system of equations:

$$\frac{x-x_C}{x_B-x_C}=\frac{y-y_C}{y_B-y_C}=\frac{z-z_C}{z_B-z_C}$$

$$(x-x_0)^2+(y-y_0)^2+(z-z_0)^2=R^2$$

Distance between points C and D:

$$L2=\sqrt{(x_D-x_C)^2+(y_D-y_C)^2+(z_D-z_C)^2}$$

The length of the DCA is equal

$$L=L1+L2$$

The sphere with radius R radiates a monochromatic wave with frequency ω and wavelength $\lambda=\frac{2\pi V_C}{\omega}$ and speed of light V_C.

At time t, the strength of the electric field (created by the DCA beam) at point A is equal to

$$E=E_0\cos(\omega(t-\frac{L}{V_C}))$$

where E_0 is strength of the incident radiation.

The projections of E (created by beam DCA) on axes X, Y and Z at point A at time t are equal to:

$$E_x=E\ cos(CA_x),\ E_y=E\ cos(CA_y),\ E_z=E\ cos(CA_z)$$

The projections of E (created by the resonator) on axes X, Y and Z at point A at time t are equal to the amount of the projections of E (created by

beams DCA), where point C passes each node of the square cells into which the resonator is divided:

$$E_x^{resonator} = \sum_{resonator} E_x \,,\; E_y^{resonator} = \sum_{resonator} E_y \,,\; E_z^{resonator} = \sum_{resonator} E_z \,.$$

The strength of electric field E (created by the resonator) at point A at time t is equal to

$$E_A^{resonator} = \sqrt{(E_x^{resonator})^2 + (E_y^{resonator})^2 + (E_z^{resonator})^2}$$

Given time change Δt, we can calculate the strength of electric field E at any point of the receiver at any point in time.

The results are output as 4-dimensional matrices (the coordinates of the point at which E is calculated, and the time):

$$E_A^{resonator} \,,\; E_x^{resonator} \,,\; E_y^{resonator} \,,\; E_z^{resonator} \,.$$

To following formula is used to account for diffraction:

$$\frac{I_\beta}{I_0} = \frac{\sin^2(\frac{\pi b}{\lambda}\sin\beta)}{(\frac{\pi b}{\lambda}\sin\beta)^2} \,,$$

where I_β is the intensity of waves propagating at an angle β, I_0 is the intensity of waves propagating at an angle β=0, b is the width of the slit, β is the angle, λ is the wavelength. Because the intensity of the wave is proportional to the square of the amplitude,

$$\frac{I_\beta}{I_0} = \frac{E_\beta{}^2}{E_0{}^2} = \frac{\sin^2(\frac{\pi b}{\lambda}\sin\beta)}{(\frac{\pi b}{\lambda}\sin\beta)^2} \,,$$

$$E_\beta = E_0 \frac{\sin\ (\frac{\pi b}{\lambda}\sin\beta)}{\frac{\pi b}{\lambda}\sin\beta} \,.$$

Thus, in the end in general we have a vector E:

$$E = E_{otr} + E_{difr} \,,$$

where E_{otr} is due to reflection, E_{difr} is due to diffraction (in the case of narrow slits).

3. CALCULATION PARAMETERS

1. The topological circuit of the Aires resonator (microprocessor) is considered a self-affine annular diffraction grating made in the form of slits with the following dimensions: $0.2 * 10^{-6}$ m x $0.8 * 10^{-6}$ m (0.2 μm x 0.8 μm, width and depth).
2. Resonator dimensions: $19.6 * 10^{-3}$ m x $19.6 * 10^{-3}$ m x $0.5 * 10^{-3}$ m (19.6mm x 19.6mm x 0.5mm).
3. The resonator interacts with the radiation of the Wi-Fi source (router) in the form of a large-diameter hemisphere (the diameter of a sphere larger than the wafer dimensions). The distance from the source to the resonator is 10 m.
4. The surface of the resonator reflects radiation (absorption is not considered), but the slits absorb (reflection in the slits is not considered).
5. Parameters of the incident radiation:
    - strength E_0= 50 (V/m) (manufacturer data).
    - frequency ω = 28 GHz.
    - field strength $E \sim \omega^2 = (28\ \text{GHz})^2 \sim 78.4$ (V/m).
    - flux density $I \sim \omega^4 = (28\ \text{GHz})^4 \sim 61.47$ (W/m^2).
6. The resonator surface is divided into square cells in increments of $h = 32 * 10^{-6}$ m (32 μm). The resulting radiation is calculated in the space above the resonator, at the nodes of a cubic lattice with step h.
7. The electromagnetic radiation interacts with the resonator for $t = 1$ s.
8. The time spent on the calculations is ~ 4320 machine-hours.

4. ALGORITHM FOR THE CALCULATION

The algorithm for the calculation generally looks like this:

1. The Aires resonator (microprocessor) with the 64P1S5G topology (Appendix 1) is taken to be at the center of the cubic matrix. To reduce the required resources, the calculations are performed for the upper half of the cubic matrix with a determination of the estimated electric field strength at each node of the lattice, and then the results are mirrored to the lower half. As a result, we obtain a matrix that is symmetric with respect to the plane on which the resonator is placed, and a cubic matrix of the results of the initial strength calculation E – " Prototype result".

2. At this stage, an additional gradation of the lattice is introduced to the cubic matrix of the 1st derivative with a 2-fold decrease in the spatial increment h ($32*10^{-6}$ m → $16*10^{-6}$ m), which makes it possible to identify internal structural relationships. The results are stored in the strength matrix *E* - "Derivative 1".

3. At this stage, an additional gradation of the lattice is introduced to the cubic matrix of the 1st derivative with a 2-fold decrease in the spatial increment h ($16*10^{-6}$ m → $8*10^{-6}$ m) again, which makes it possible to identify internal structural relationships. The results are stored in the strength matrix *E* - "Derivative 2".

4. At this stage, an additional gradation of the lattice is introduced to the cubic matrix of the 1st derivative with a 2-fold decrease in the spatial increment h ($8*10^{-6}$ m → $4*10^{-6}$ m) again, which makes it possible to identify internal structural relationships. The results are stored in the strength matrix *E* - "Derivative 3".

5. Next, "Derivative 3" with a center at the origin (center of the resonator) and radius R_1 (radius of the topological circuit) is projected by distance R_1 along 1026 radii (the number of axes of fractalization of the spatial resonator whose 2D profile is the specimen with the 64P1S5G topology under study), and at the nodes of the lattice we sum the results (1027 spheres). In the end, we obtain calculated values of the superposition, fractalized along 1026 axes, that determines the spatial distribution of the electric field strength, geometrically comprising a sphere of radius $R_2 = 2 * R_1$, which we denote as "Derivative 4".

5. RESULTS AND DISCUSSION

For the most complete and adequate understanding of the processes, the model was initially considered and calculations of the incident electromagnetic radiation's interaction with the resonator surface and the diffraction response that was induced on it. The resonator is a ring with a radius of $2.424*10^{-3}$ m with given slit parameters (depth - $0.2*10^{-6}$ m, width - $0.8*10^{-6}$ m), which is the basic symmetric structural element of the topology of the Aires 64P1S5G resonator (microprocessor). The results are shown in Fig. 8.

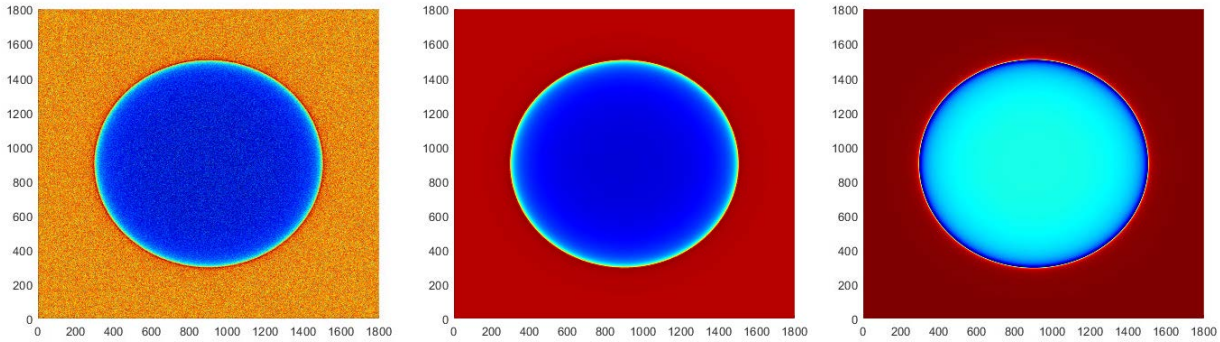

a) *b)* *c)*

Fig. 8. Diffraction response on the 1s ring: a) $\nu = 28 * 10^{21}$Hz (gamma radiation), b) $\nu = 5.5 * 10^{14}$Hz (green spectrum of the Sun), c) $\nu = 28 * 10^{9}$Hz (Wi-Fi 5G radiation)

As can be seen from Fig. 8, the interaction produces an annular spectrogram. In the case of gamma radiation, a regular fractal structure is formed inside the ring as a result of integral interaction of waves (superposition) (Fig. 9), and outside - analogous to natural objects (Fig. 10).

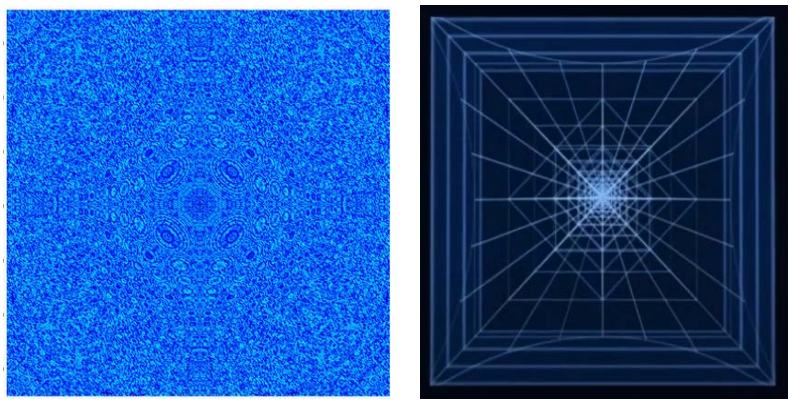

Fig. 9. Fragment of the image of the central zone from Fig. 8a)

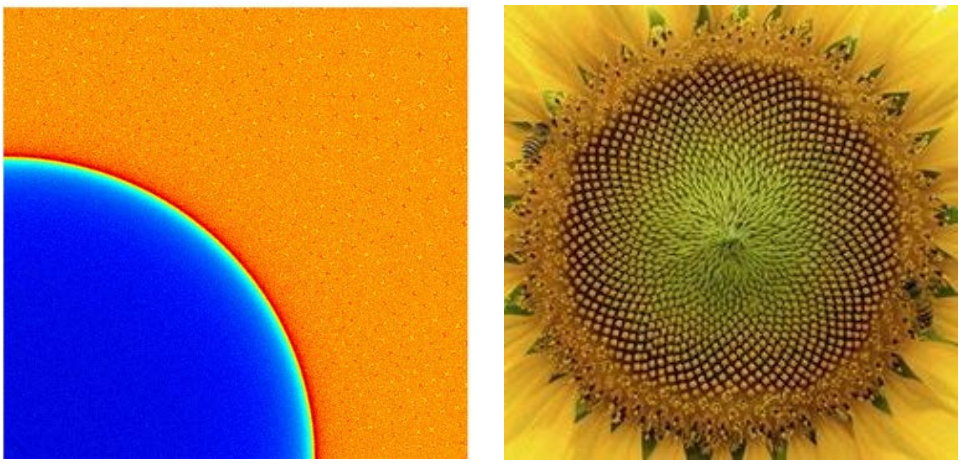

Fig. 10. Fragment of the image from Fig. 8a) and a photo of a sunflower

The ring shape has a specific feature in that, since its surface is curved and has a focal point located at the center of the ring, an impulse striking the interior begins to move along a trajectory that intersects this point and, upon reaching the opposite surface of the ring, is reflected and returned, again intersecting the focal point.

Thus, the appearance of an absolutely adequate counter function begins resonant self-generation of the potential with the transformation of the wave spectrum in the form of “Fresnel rings”.

In turn, electrons begin to move along the annular slit, which provokes the formation of an opposing wave stream, and when their phases coincide, a standing wave is formed.

Stage 1 of the calculation - "Prototype result".

In accordance with the algorithm, the calculations were performed in 5 stages. The result of the first stage is a matrix of the strength of the electric field E over the resonator. At a frequency of 28 GHz there is a secondary wave occurrence (Figs. 11, 12).

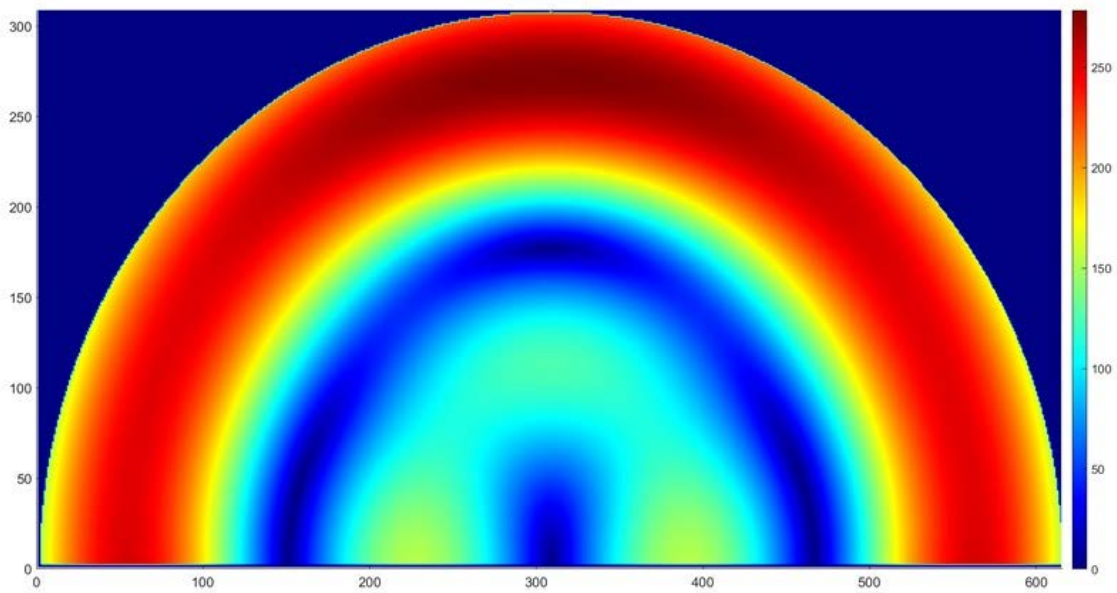

Fig. 11. Distribution of field strength E over the resonator at stage 1 of the calculations (vertical section through the center)

The distribution of the electric field strength occurs symmetrically from the center of the resonator, where E = 0.82 (V/m), to the edges, where the strength reaches E = 253.16 (V/m) (Fig. 12).

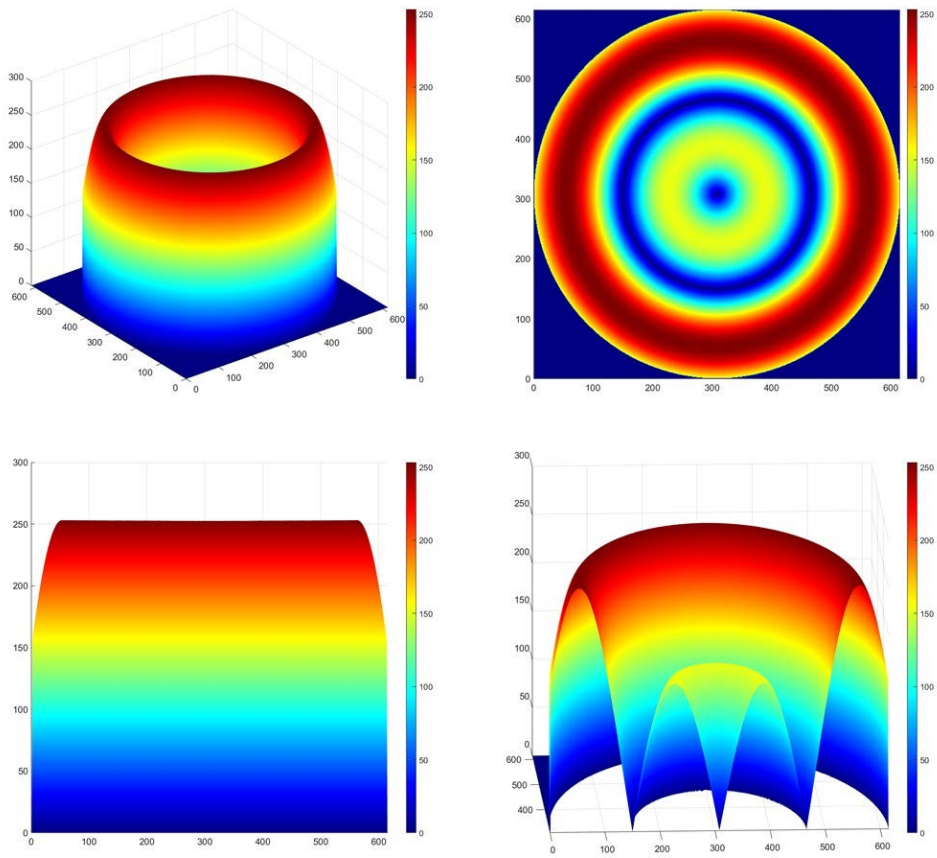

*Fig. 12. Distribution of field strength E over the resonator at stage 1 of the calculations (horizontal section at height h = 32*10^{-6} m), range E = 0.82 ÷ 253.16 (V/m)*

Stage 2 of the calculation - " Derivative 1".

After introducing additional gradation into the existing lattice (step = $16*10^{-6}$ m), a cubic matrix of field strength was obtained, with an increase in the maximum strength amplitude to the value E = 555.64 (V/m) relative to the initial matrix obtained at stage 1 of calculation (Figs. 13-15).

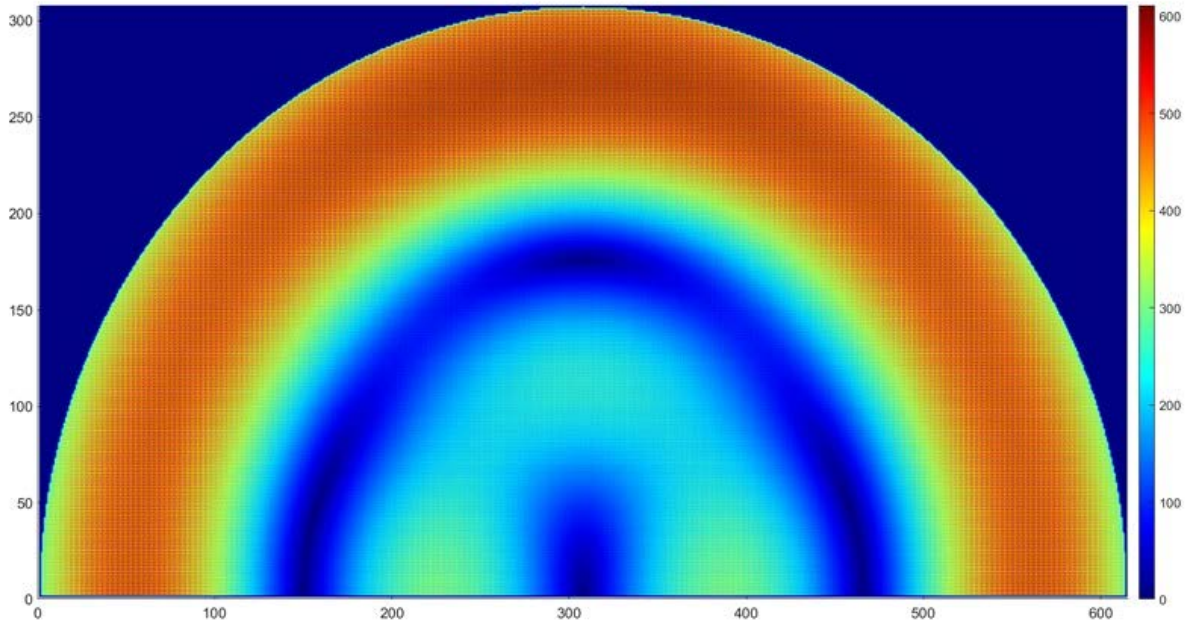

Fig.13. Distribution of field strength E over the resonator at stage 2 of the calculations (vertical section through the center)

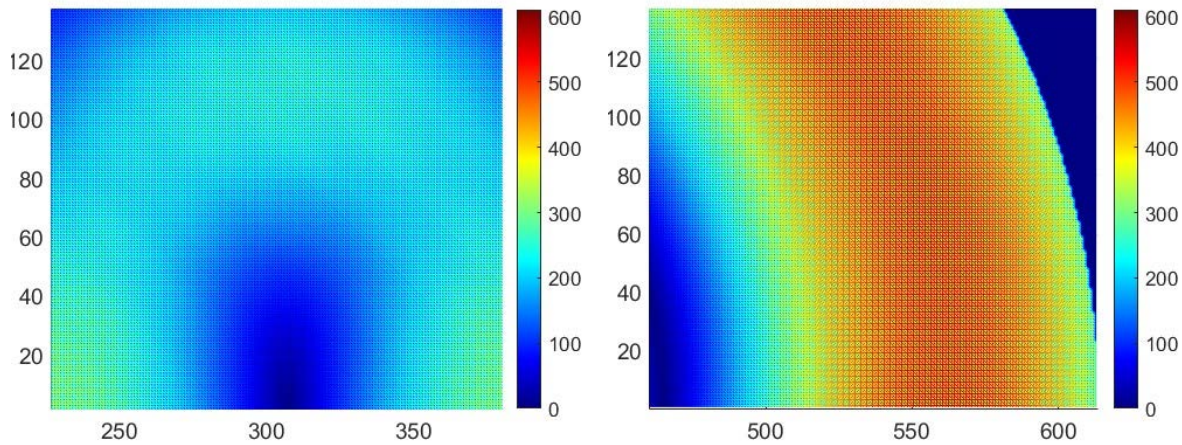

Fig. 14. Fragments of the image presented in Fig. 13 at a scale of 4:1

The appearance of a regular system of strength maxima and minima (Figs. 13-16) reflects the new functional nature of the electromagnetic field's emerging raster lattice over the Aires 64P1S5G resonator (microprocessor), which begins working as a differentiating system.

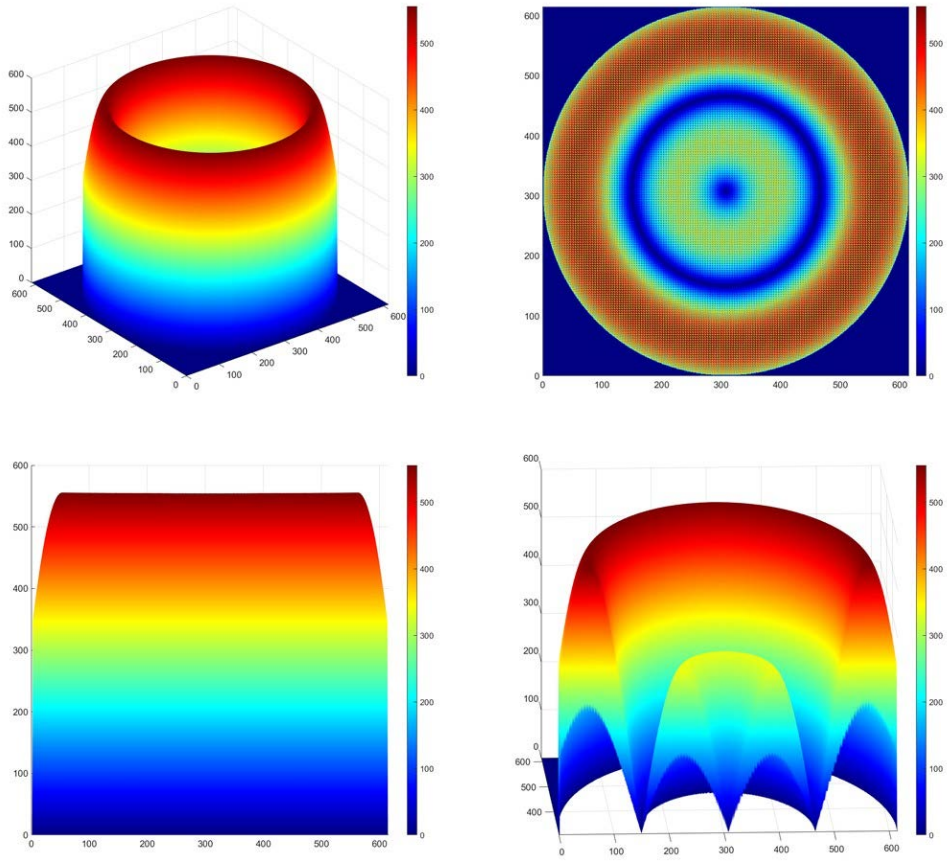

*Fig. 15. Distribution of field strength E over the resonator at stage 2 of the calculations (horizontal section at height h = 32*10^{-6} m), range E = 0.82 ÷ 555.64 (V/m)*

For greater clarity of the arising effect, Fig. 16 shows fragments of the image of the distribution of strength E, presented in Fig. 15, with different scales.

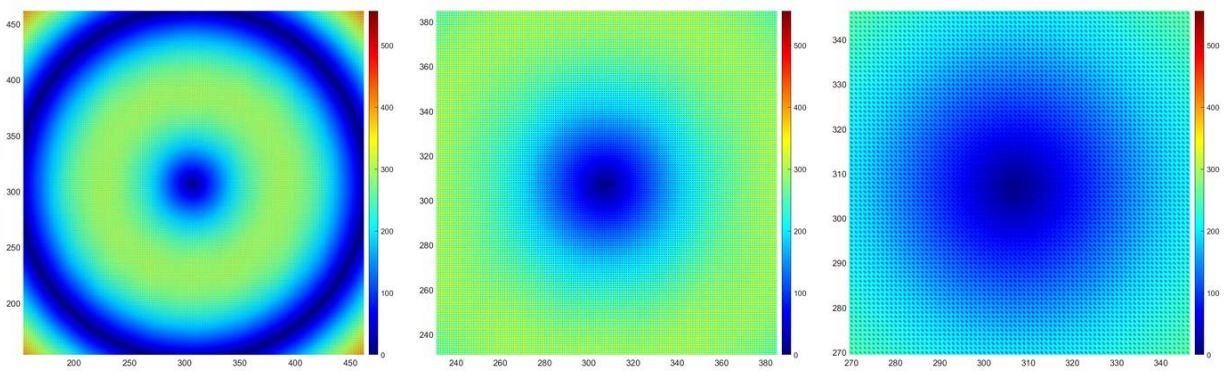

а) *б)* *в)*

Fig. 16. Fragments of the image presented in Fig.15:
a) at 2:1 scale, b) at 4:1 scale, c) at 8:1 scale

Stage 3 of the calculation - " Derivative 2".

After introducing the next additional gradation into the existing lattice (step = $8*10^{-6}$ m), a cubic matrix of field strength was obtained, with an increase in the maximum strength amplitude to the value E = 1801.65 (V/m) relative to the initial matrix obtained at the 1st stage of calculation (Figs. 17-19).

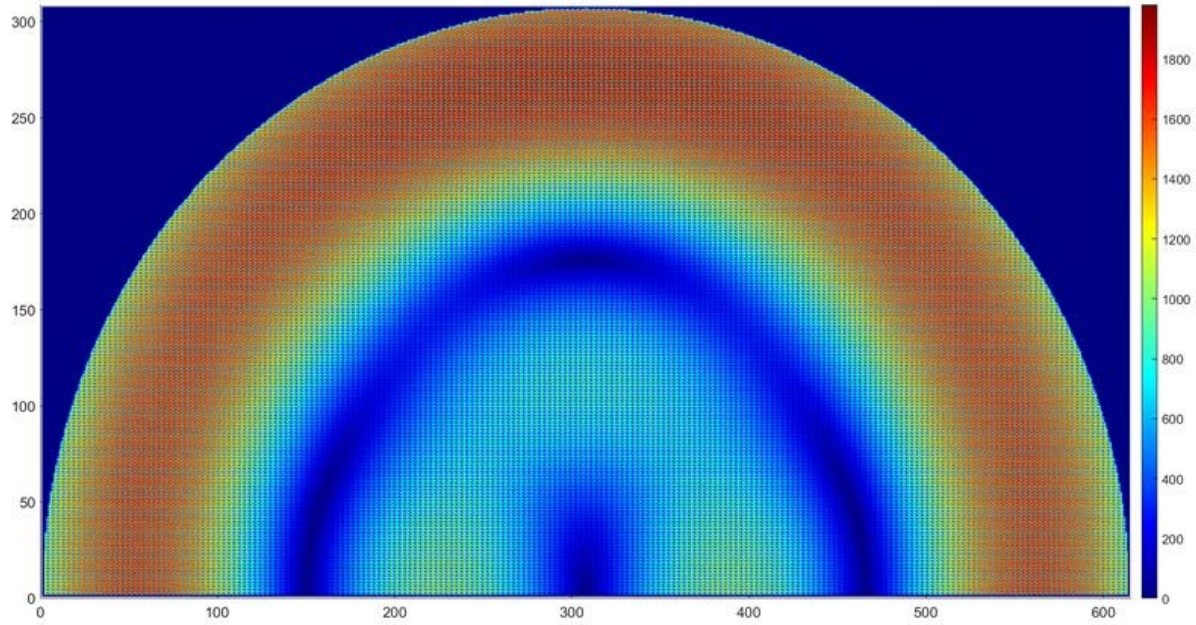

Fig. 17. Distribution of field strength E over the resonator at stage 3 of the calculations (vertical section through the center)

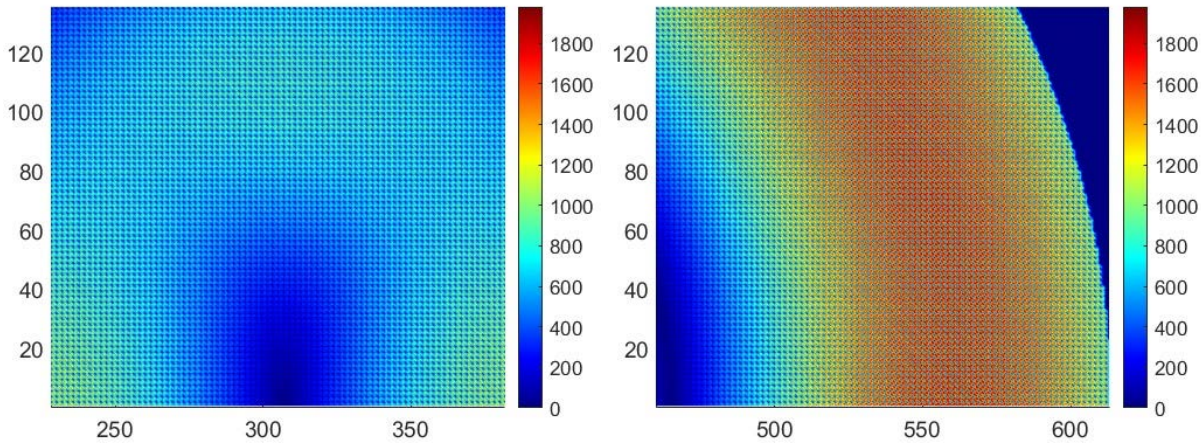

Fig. 18. Fragments of the image presented in Fig. 17 at a scale of 4:1

The appearance of a two-level regular system of strength maxima and minima (Figs. 17-22) reflects the new functional nature of the electromagnetic field's emerging raster lattice over the Aires 64P1S5G resonator (microprocessor), which begins working as a differentiating system.

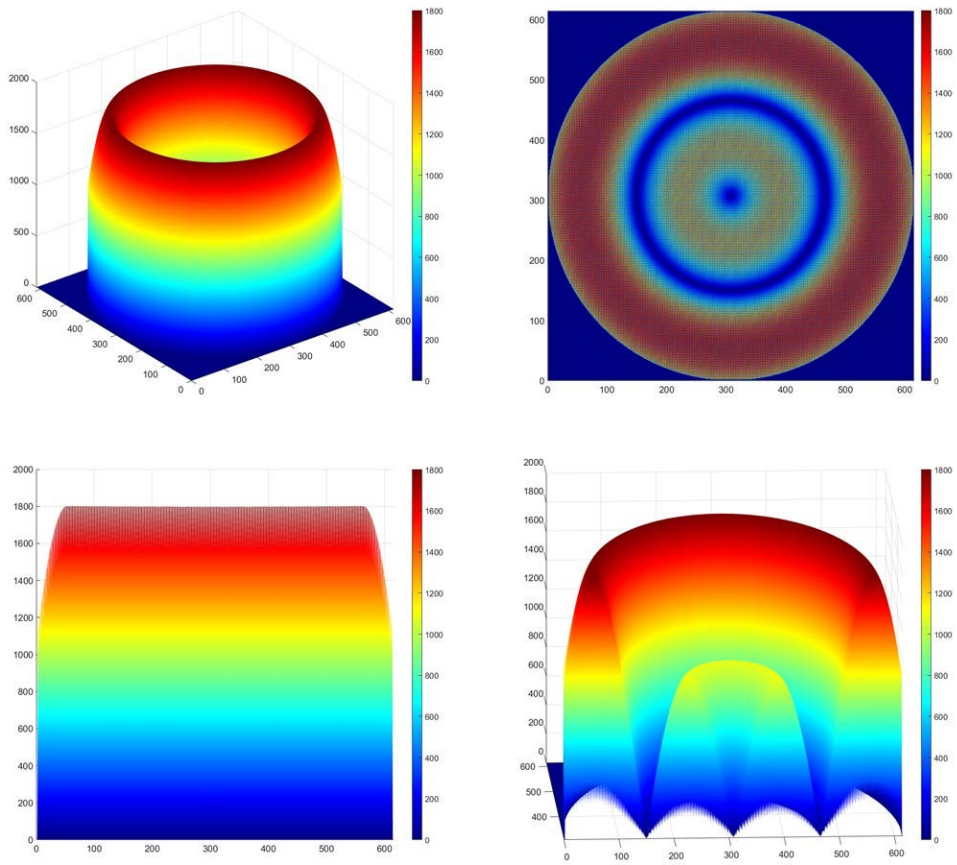

*Fig. 19. Distribution of field strength E over the resonator at stage 3 of the calculations (horizontal section at height of h = 32*10^{-6} m), range E = 0.82 ÷ 1801.65 (V/m)*

For greater clarity of the arising effect, Figs. 20-22 show fragments of the image of the distribution of strength E, presented in Fig. 19, with different scales.

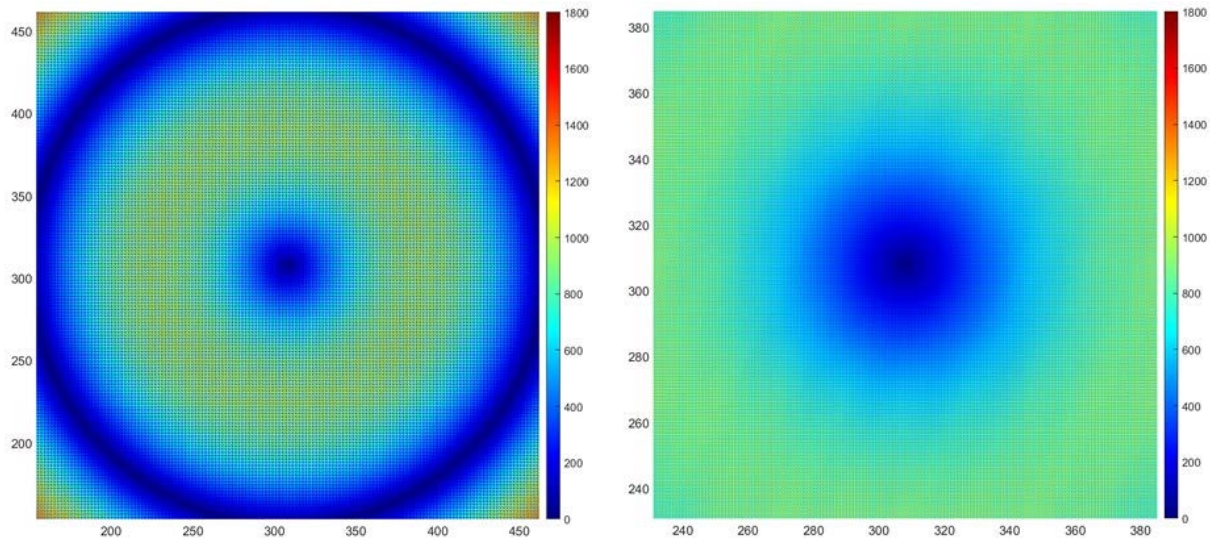

a) *b)*

Fig. 20. Fragments of the image presented in Fig. 19:
a) at 2:1 scale, b) at 4:1 scale

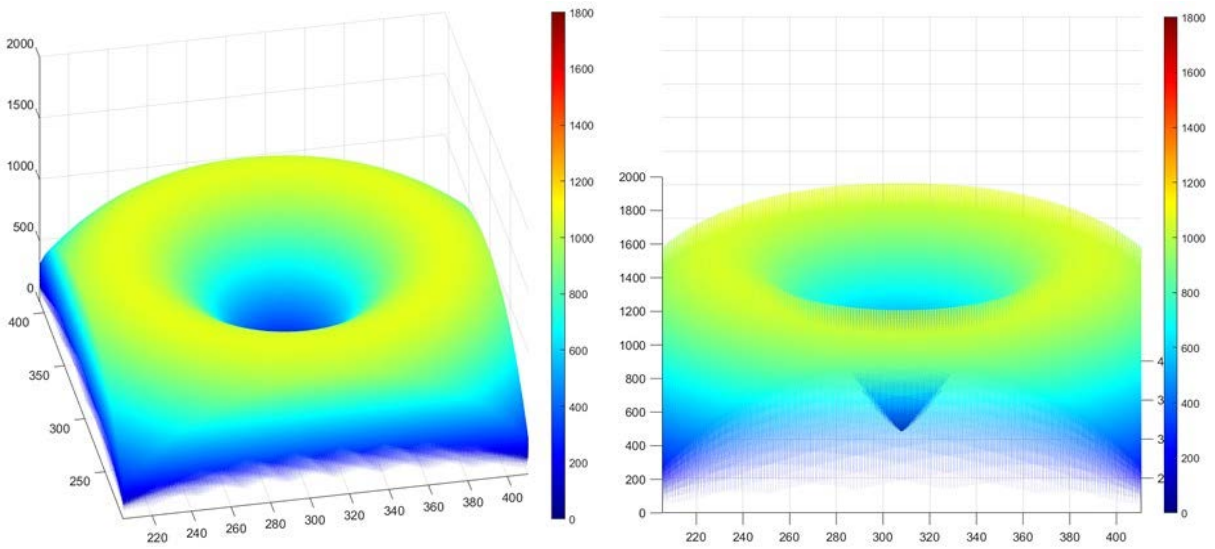

Fig. 21. Fragments of the image presented in Fig. 19 at 3:1 scale

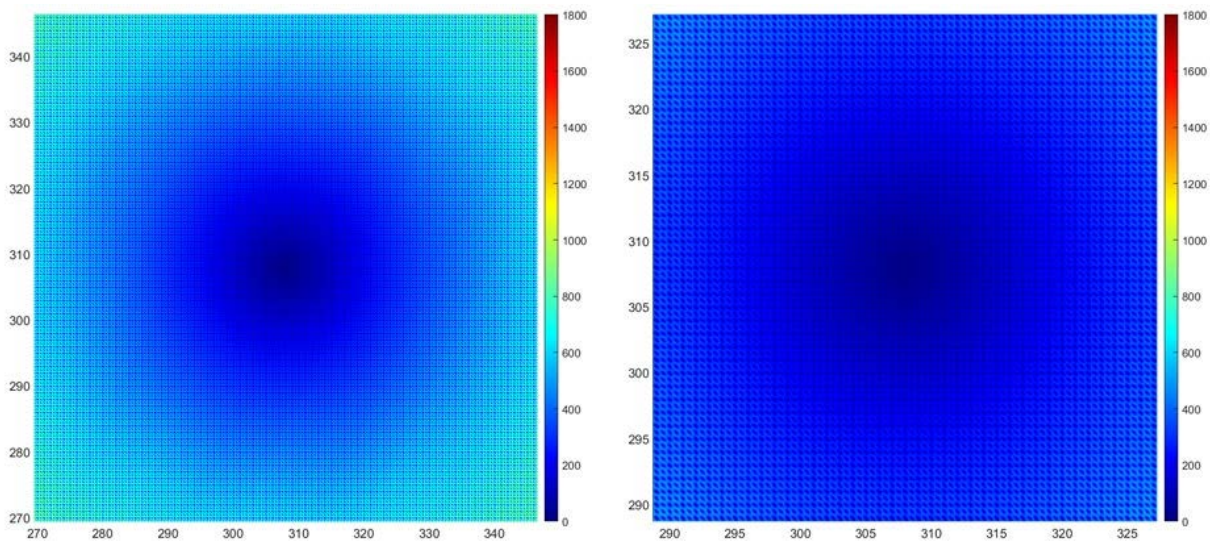

a) *b)*

Fig. 22. Fragments of the image presented in Fig. 19
a) at 8:1 scale, b) at 16:1 scale

Stage 4 of the calculation - " Derivative 3".

After introducing the last additional gradation into the existing lattice (step = $4*10^{-6}$ m), a cubic matrix of field strength was obtained, with an increase in the maximum strength amplitude to the value E = 9469.56 (V/m) relative to the initial matrix obtained at the first calculation stage (Figs. 23-25).

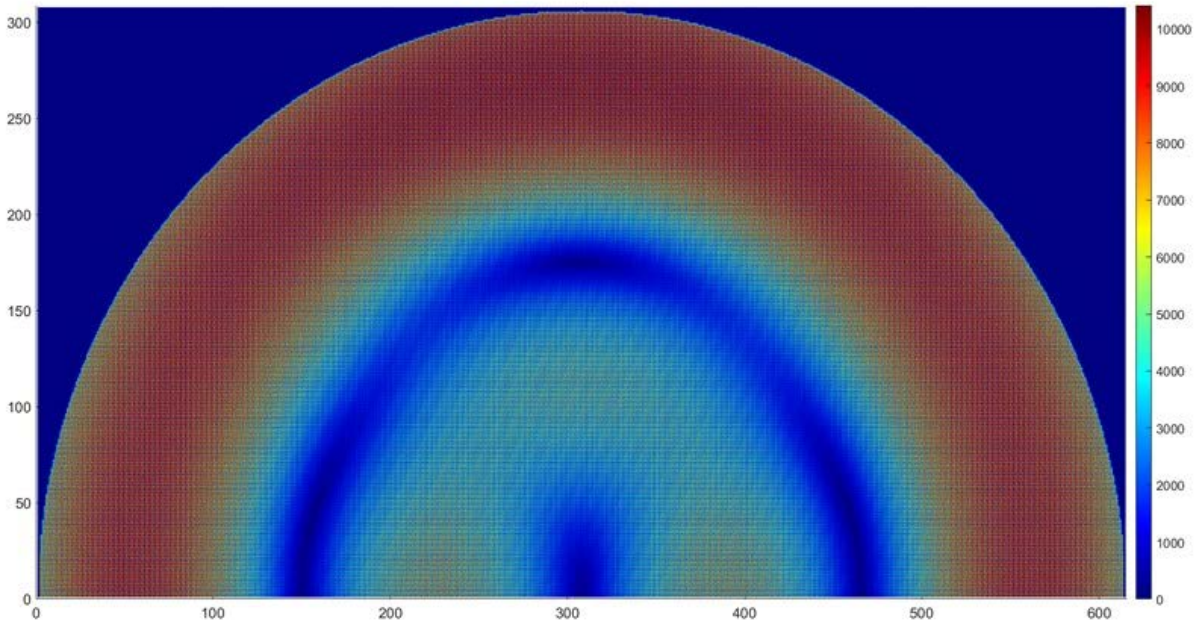

Fig. 23. Distribution of field strength E over the resonator at stage 4 of the calculations (vertical section through the center)

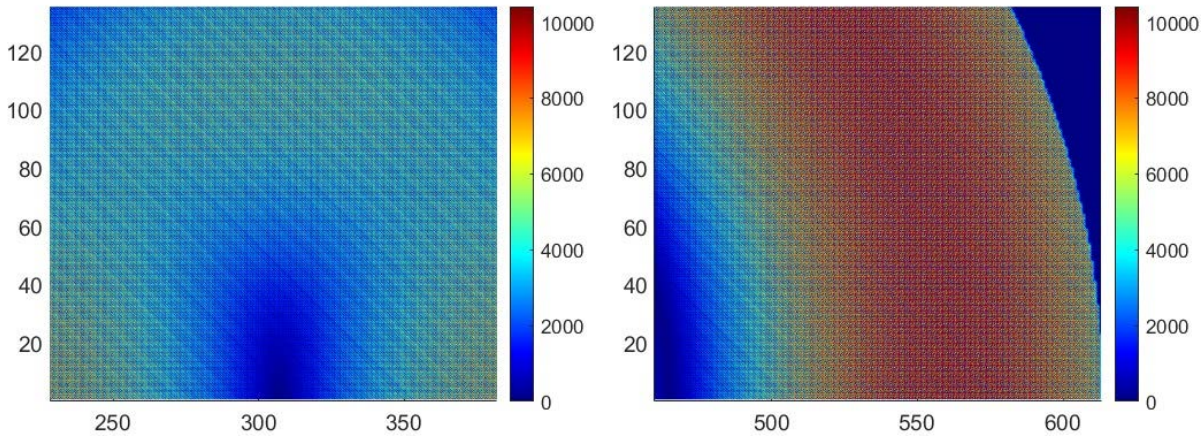

Fig. 24. Fragments of the image presented in Fig. 23 at a scale of 4:1

The appearance of a three-level regular system of maxima and minima of strength (Figs. 23-29) reflects the new functional nature of the emerging raster lattice of the electromagnetic field over the resonator (microprocessor) Aires 64P1S5G, which begins to work as a differentiating system.

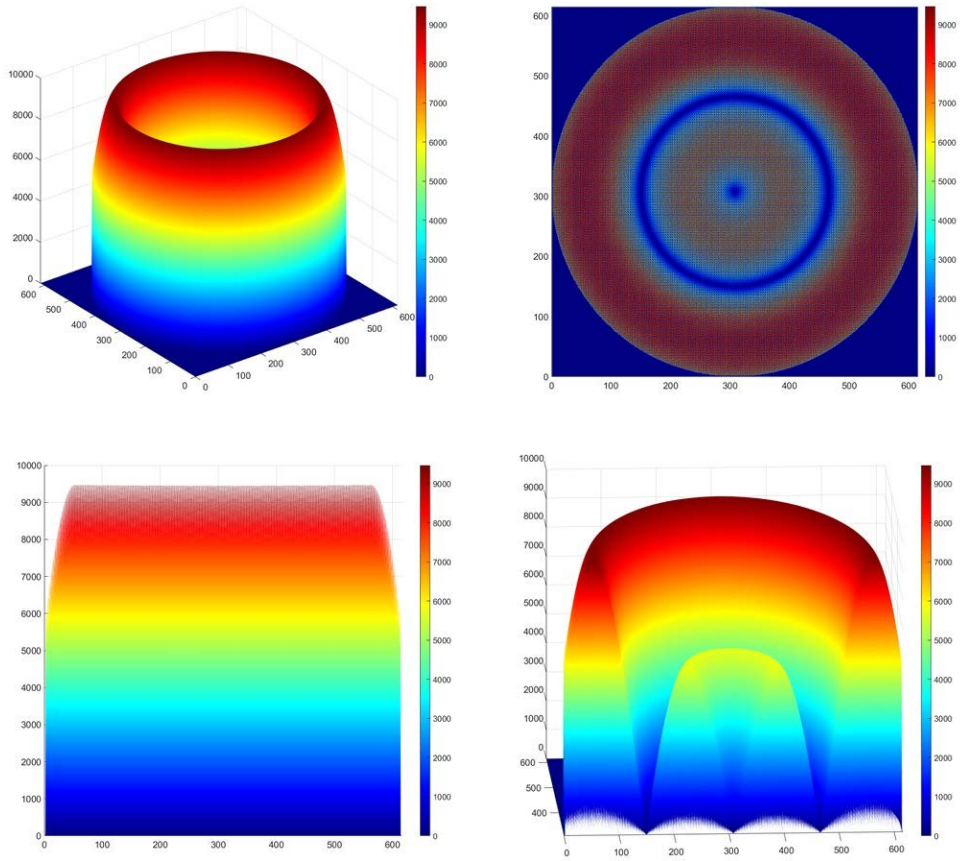

*Fig. 25. Distribution of field strength E over the resonator at stage 4 of the calculations (horizontal section at height of h = 32*10^{-6} m), range E = 0.82 ÷ 9469.56 (V/m)*

For greater clarity of the resulting effect, Figs. 26-29 show fragments of the image of the distribution of strength E presented in Fig. 25, with different scales.

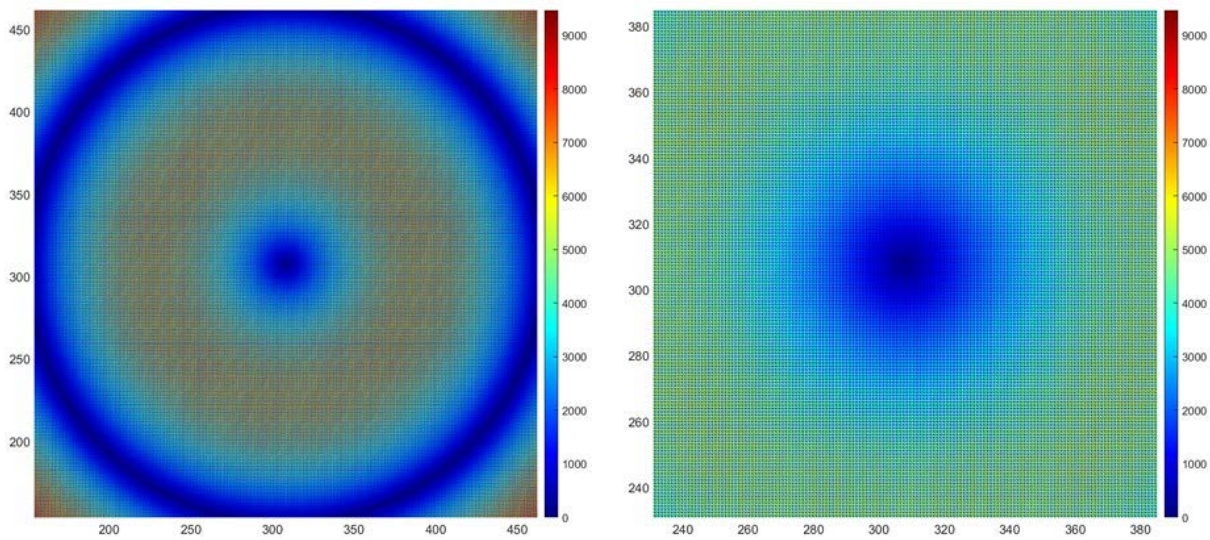

a) *b)*

Fig. 26. Fragments of the image presented in Fig. 25
a) at 2:1 scale, b) at 4:1 scale

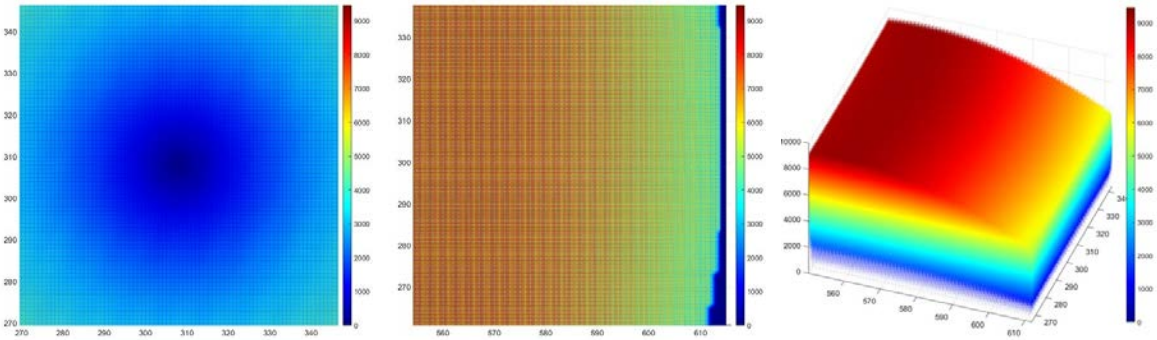

Fig. 27. Fragments of the image presented in Fig. 25 at a scale of 8:1

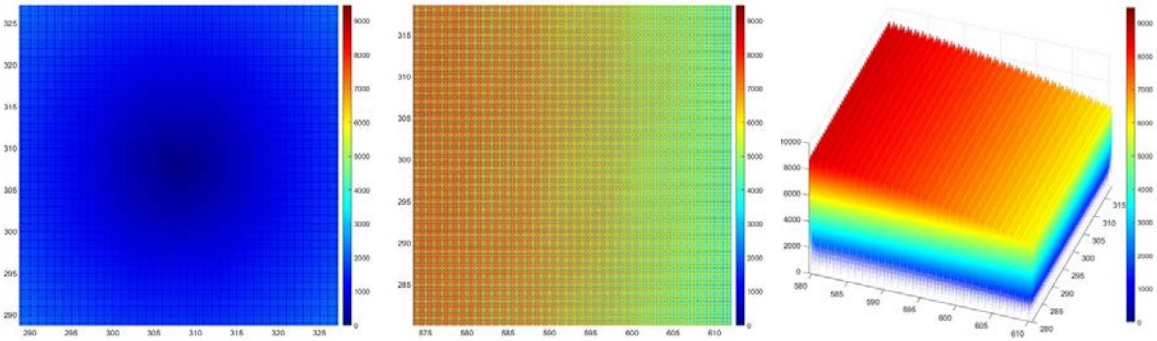

Fig. 28. Fragments of the image presented in Fig. 25 at a scale of 16:1

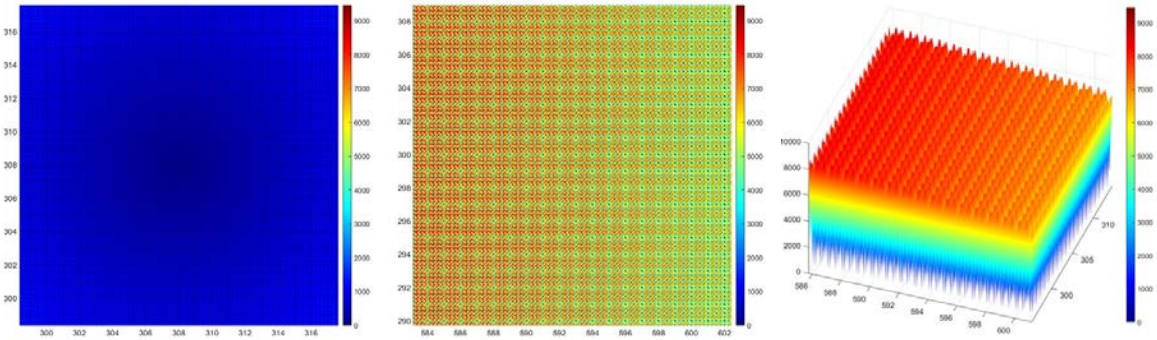

Fig. 29. Fragments of the image presented in Fig. 25 at a scale of 32:1

Stage 5 of the calculation - " Derivative 4".

Since an orthogonal coordinate system is used in modeling, irrational (non-linear) parameter values corresponding to the √2 coefficient (diagonals of square lattice) occur in the angular zones used for construction. To limit the irrationality coefficient, and correspondingly the calculation time, an additional coordinate system unfolded by 45° with respect to the basic one is introduced, which leads to the appearance of octahedral structural compositions fixed simultaneously in two coordinate systems (Fig. 30).

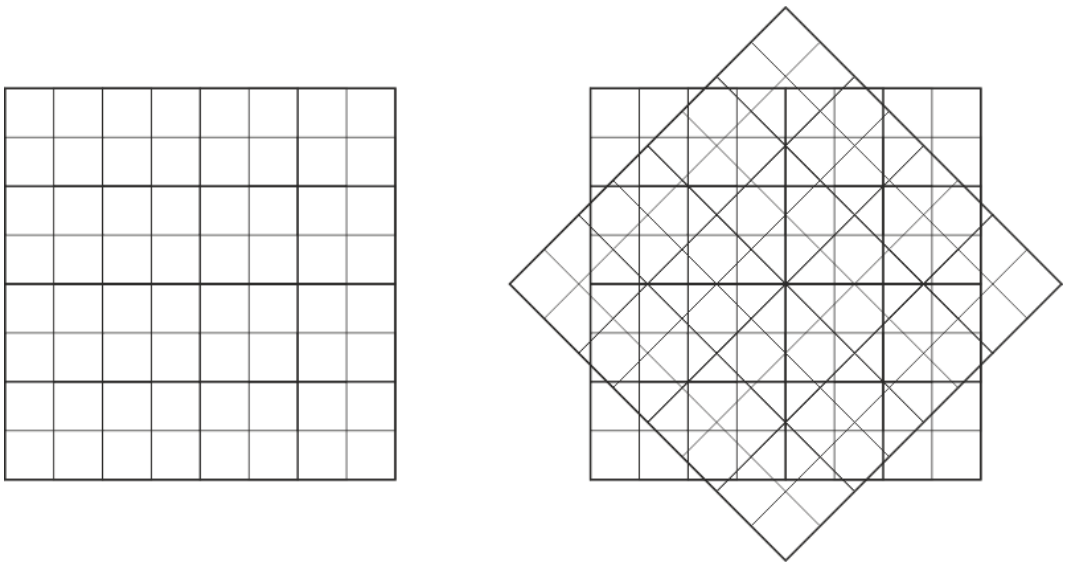

a) *b)*

Fig. 30. a) Standard orthogonal coordinate system and
b) a complex of 2 coordinate systems rotated by 45° relative to each other.

Thus, we can make the assumption that the introduction of additional coordinate systems unfolded by a certain angle allows us to proceed to the consideration and fixation of the parameters of multidimensional categories in the data array, essentially converting the general complex of coordinate systems into polar form without the need to transform it using the corresponding mathematical functions.

During the calculations of stage 5, the distribution of strength E and intensity I of the electromagnetic field in three-dimensional space was obtained (Fig. 31-36).

In the central zone appears:

- A maximum of strength followed by a sharp decrease over the central point of the circuit: $E = 3.44*10^{3} \div 2.3*10^{-3}$ (V/m) (Figs. 31-32);
- A maximum of intensity followed by sharp decrease over the central point of the circuit: $I = 1.18*10^{7} \div 5.13*10^{-6}$ (W/m^2) (Figs. 34-35).

Thus, a pronounced tendency of electromagnetic field characteristics to the amplitude minimum above the center of the circuit is clearly visible.

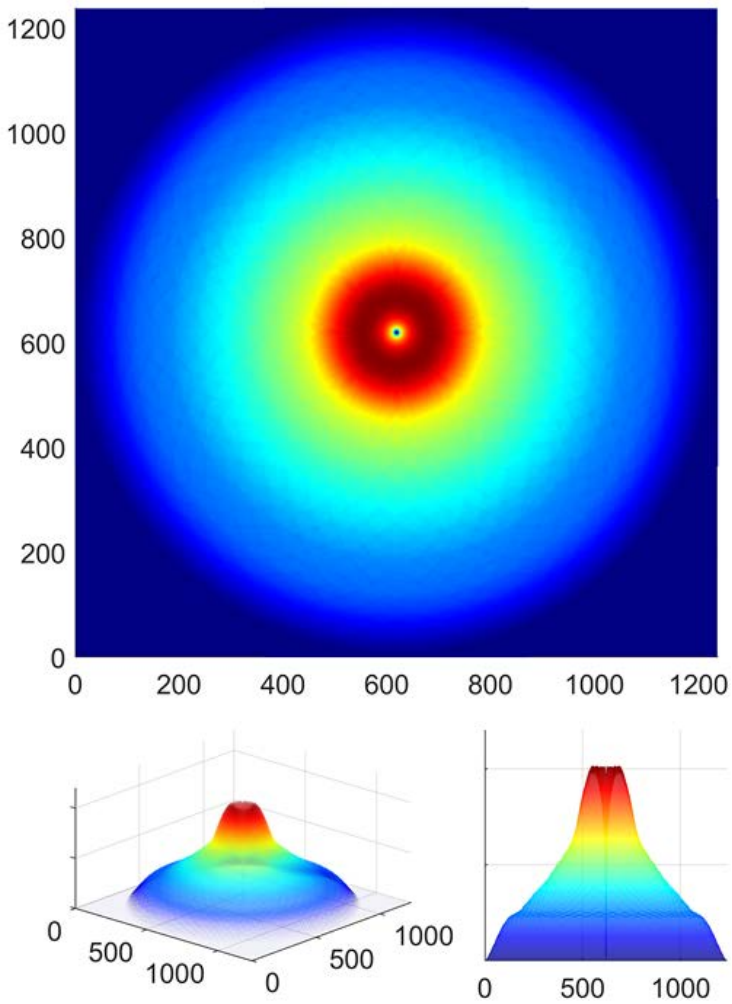

*Fig. 31. Distribution of strength E over the resonator at the level of h = 32*10^{-6} m in different projections at the 5th stage of the calculations.*

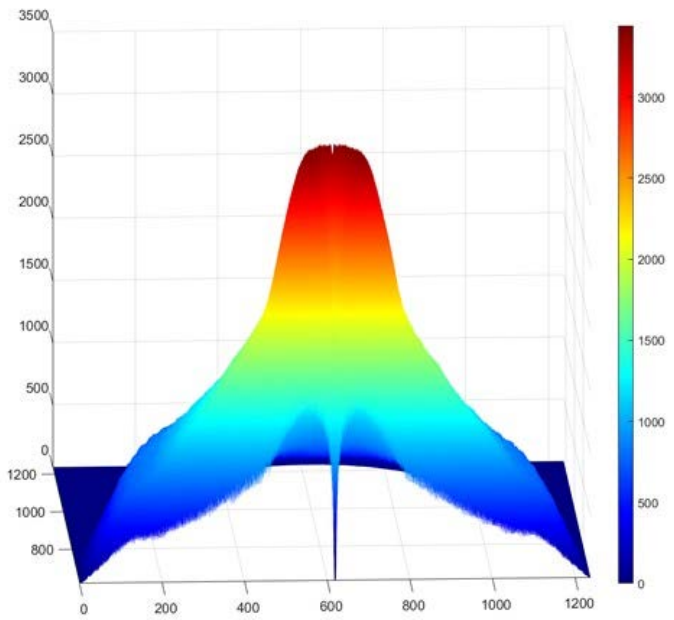

*Fig. 32. Distribution of strength E over the resonator at the level of h = 32*10^{-6} m, range E = 2.3*10^{-3} ÷ 3.44*10^{3} (V/m). Central section.*

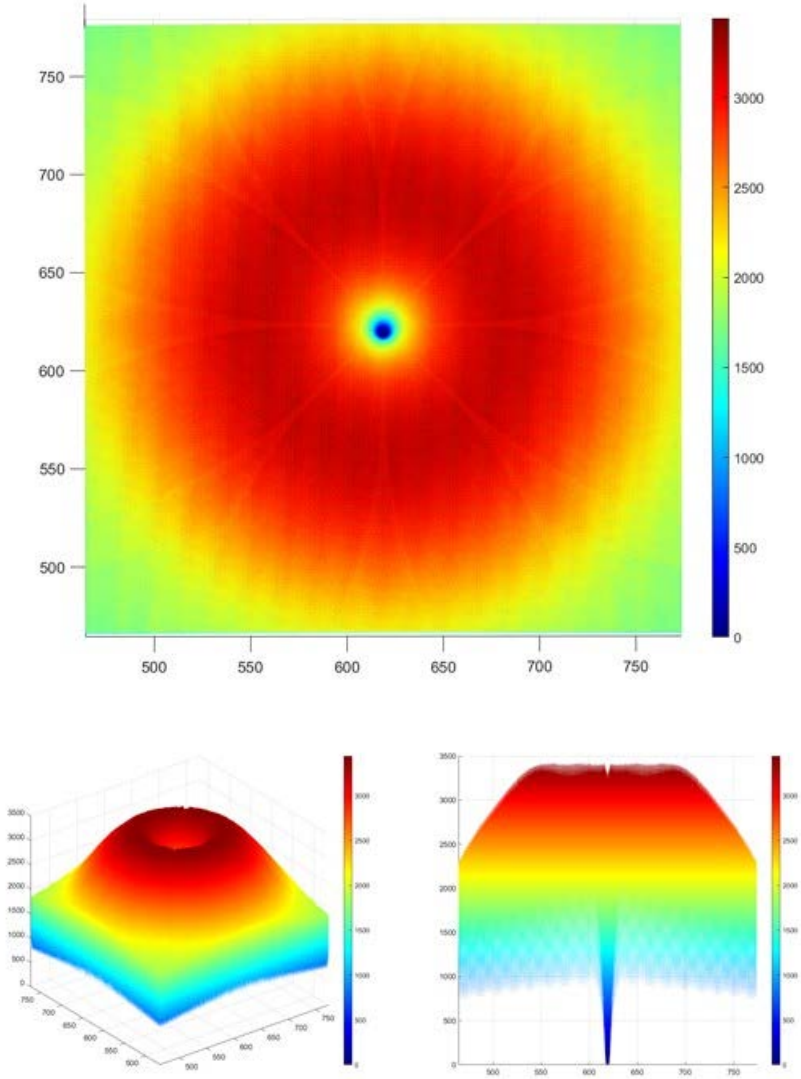

*Fig. 33. Distribution of strength E (V/m) over the resonator in different projections at the level of h = 32*10^{-6} m, at 4:1 scale.*

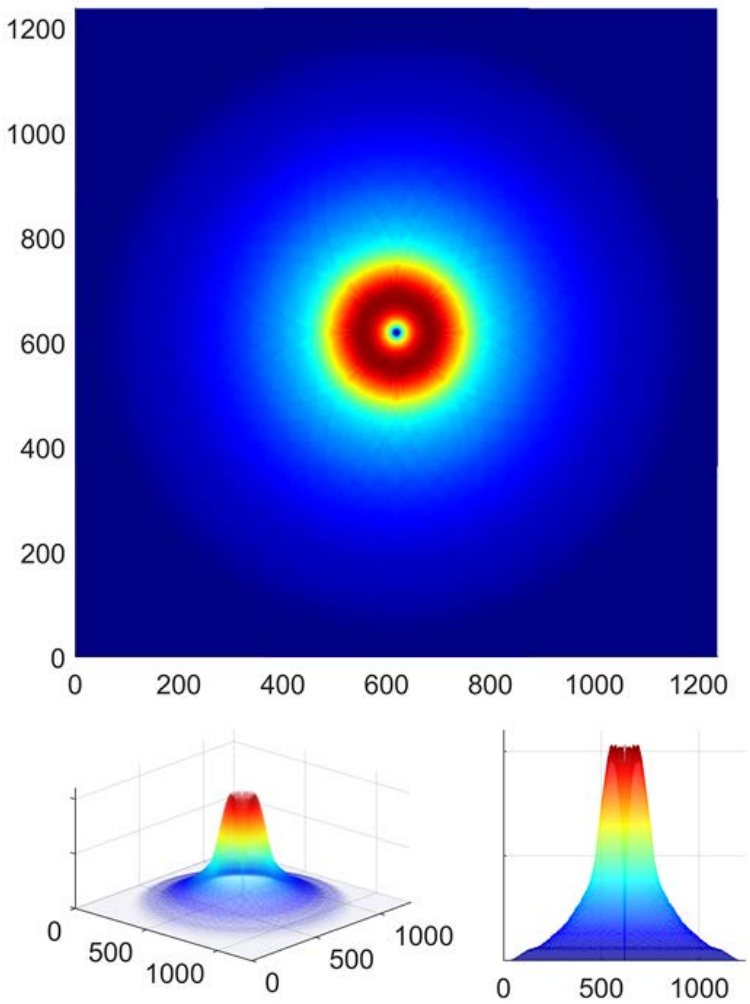

*Fig. 34. Distribution of intensity I over the resonator at the level of h = 32*10^{-6} m in different projections at the 5th stage of the calculations.*

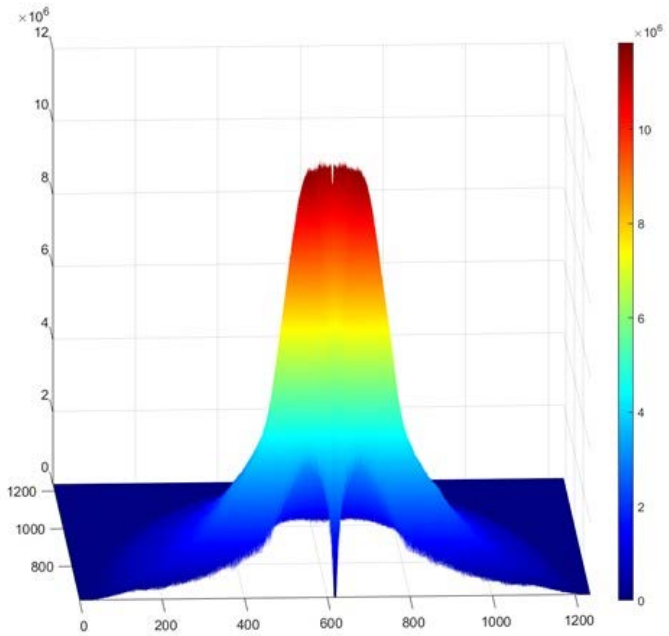

*Fig. 35. Distribution of intensity I over the resonator at the level of h = 32*10^{-6} m, range I = 5.13*10^{-6} ÷ 1.18*10^{7} (W/m^{2}). Central section.*

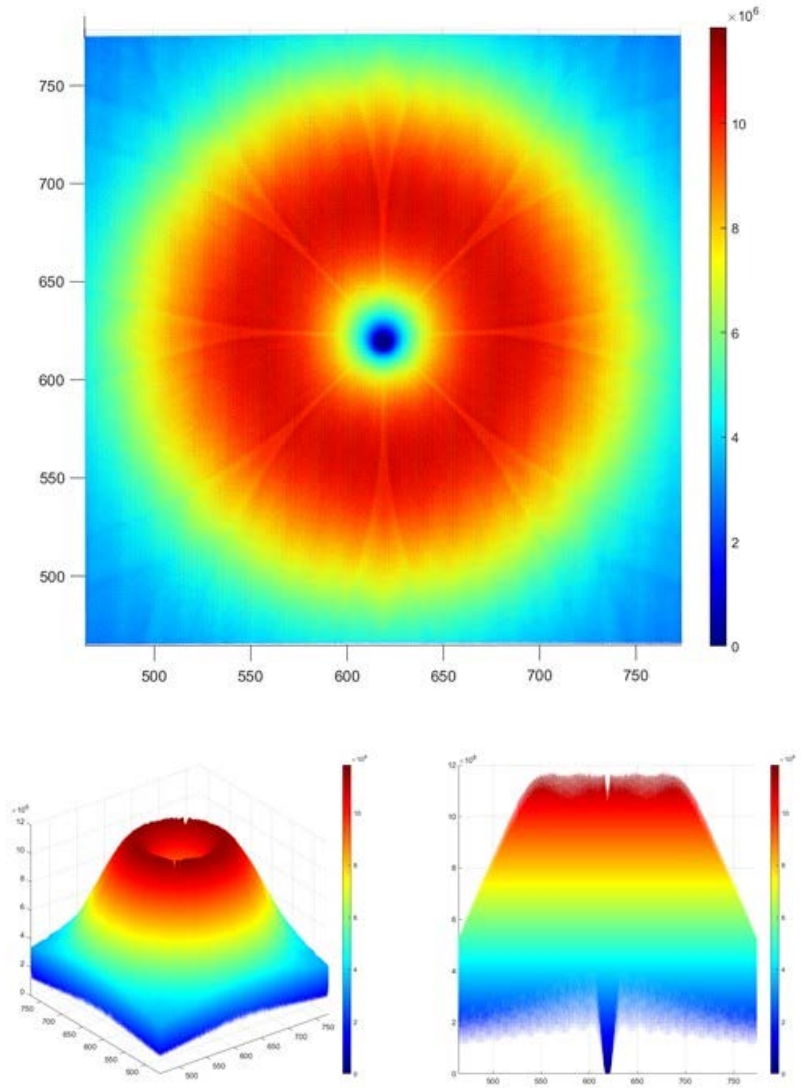

*Fig. 36. Distribution of intensity I (W/m^2) over the resonator in different projections at the level of h = 32*10^{-6} m, at 4:1 scale.*

As can be seen from Figs. 31-36, when approaching the center of the circuit, the strength *E* increases, reaching its maximum values in the immediate vicinity of the center, as well as the energy flux density *I*. And in the very center, as a result of the counteraction of potentials of the ring of strength, when their values are multiplied, there is a sharp change in the characteristics of the electromagnetic field: the strength tends to a maximum, and the amplitude approaches zero. Thus, the circuit's central zone is analogous to the point of singularity in quantum physics, i.e. the energy density there is as high as possible, and the amplitude tends to zero, which corresponds to the previously presented the matching principle expressed by the formula (1),

$$\sum_{k=1}^{n} X^k + \sum_{k=1}^{n} Y^k + \sum_{k=1}^{n} Z^k + \cdots + \sum_{k=1}^{n} N^k \to 0$$

which also implies the formation of a resonant field analogous to the intrinsic topology of the resonator.

A consequence of this response is a redistribution of the field energy flux density *I* with its nonlinear growth from the edges to the center of the resonator with a difference of $\Delta I \sim 2.3*10^{12}$ times: from $I_{min} = 5.13*10^{-6}$ (W/m^2) to $I_{max} = 1.18*10^7$ (W/m^2).

Further, within the ring of maximum response intensity, a counter resonance forms along its diameters, causing the values of the potentials participating in this process to be multiplied. As a result of counter-harmonization with respect to amplitudes, frequencies, phases, and the radiation pattern, there is a maximally neutral zone in the center and, since an active potential always redistributes from zones of maximum amplitude activity to a neutral zone, the potential density at the central point increases sharply and is constantly maintained, forming a stationary field, and the amplitude tends to zero, which initiates the singularity phenomenon. As a result, the focal point of the vector interaction of all processes with a common potential emerges at the center:

$$(I_{max})^2 = (1.18*10^7)^2 = 1.39*10^{14} \text{ (W/m}^2\text{)}.$$

Since the energy flux density of the field is proportional to the fourth power of the frequency: $I \sim \omega^4$, then the response frequency will also change: $\Delta\omega \sim \sqrt[4]{\Delta I} = \sqrt[4]{2.3*10^{12}} = 1231.49$, i.e. in 1231.49 times will increase with respect to the original 28 GHz parameter and will be 34.48 THz.

Thus, the directional harmonization of the wave processes with respect to amplitudes, phases, frequency, and the interaction diagram of the resonator's annular fractal topology initiates a stationary, maximally coherent point structure of high density with a minimum electric field intensity, which indicates the high neutrality of this zone.

In this case, the redistribution is not smooth and monotonic, but occurs in accordance with the profile features of the resonator's topological structure. Due to these features, the shape of the emerging field (electromagnetic superposition) over the resonator takes the form of a complex spatial hologram, tending toward multilevel symmetry and consisting of a large number of regular interpenetrating spherical surfaces of sizes that are multiples of one another and determined by

the fractal structure and the dimensions of the annular grooves on the surface of the resonator.

Figures 37-67 show the distribution of strength *E* and intensity *I* arising from the resonator of the field reflex with a height of $19.616*10^{-3}$ m in various horizontal sections. For clarity, the height step varies from 40h (1.28 mm) to 10h (0.32 mm) from the resonator surface.

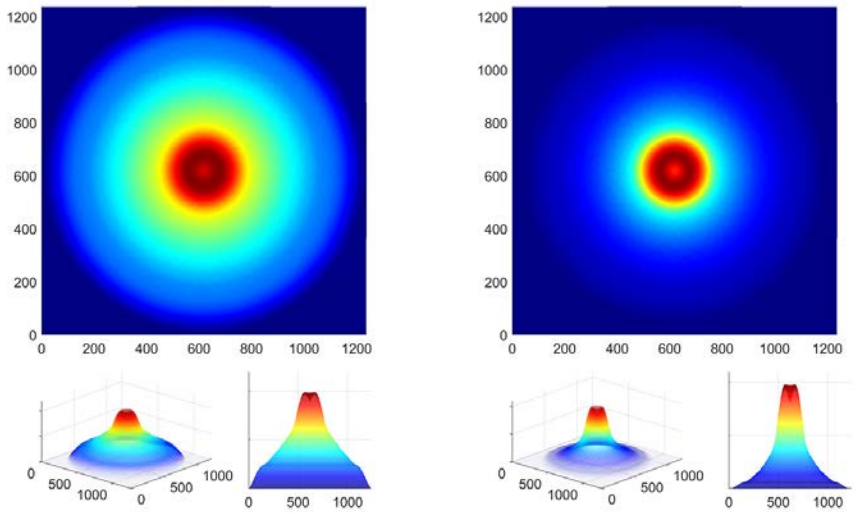

Fig. 37. Strength E (on the left) and intensity I (on the right) at level 40h ($1.28*10^{-3}$ m)

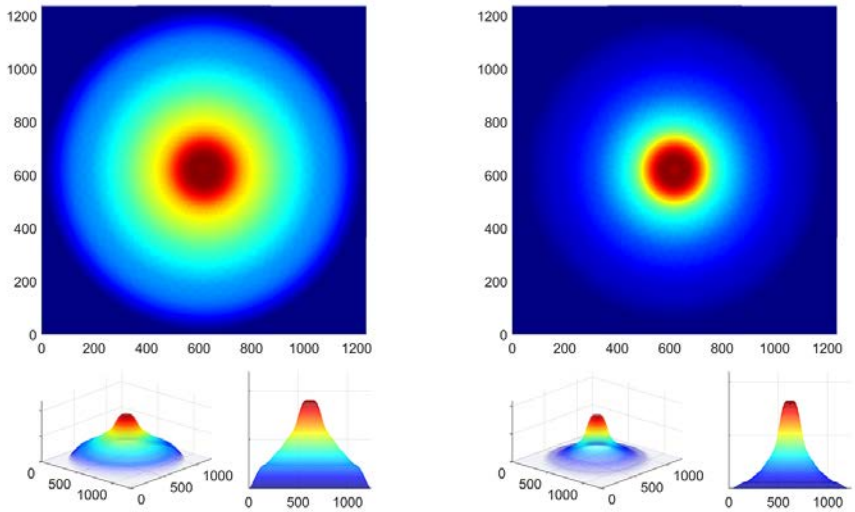

Fig. 38. Strength E (on the left) and intensity I (on the right) at level 80h ($2.56*10^{-3}$ m)

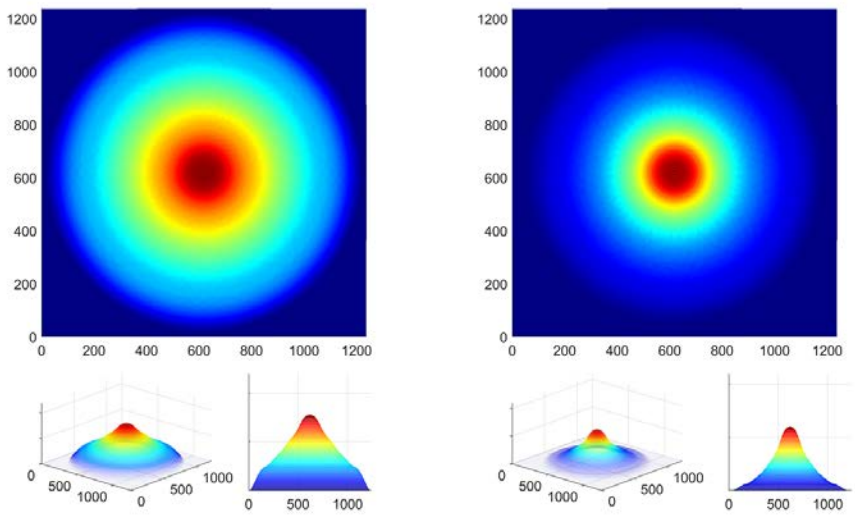

*Fig. 39. Strength E (on the left) and intensity I (on the right) at level 120h (3.84*10^{-3} m)*

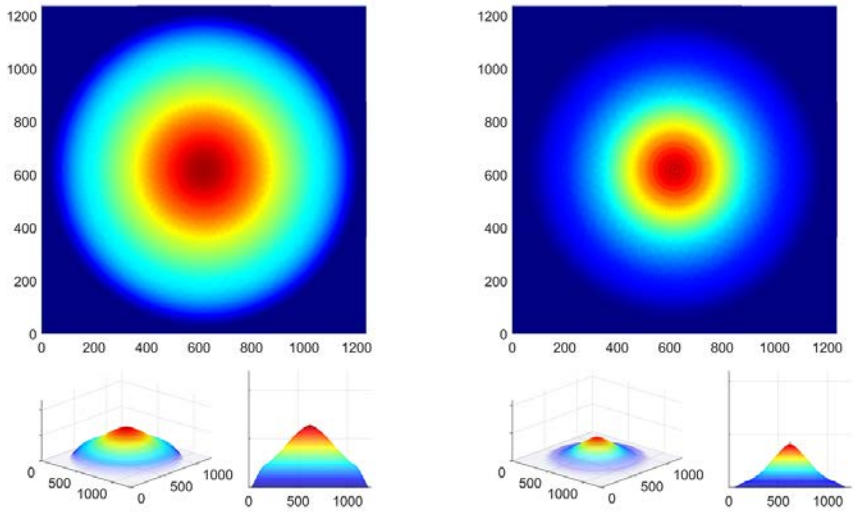

*Fig. 40. Strength E (on the left) and intensity I (on the right) at level 160h (5.12*10^{-3} m)*

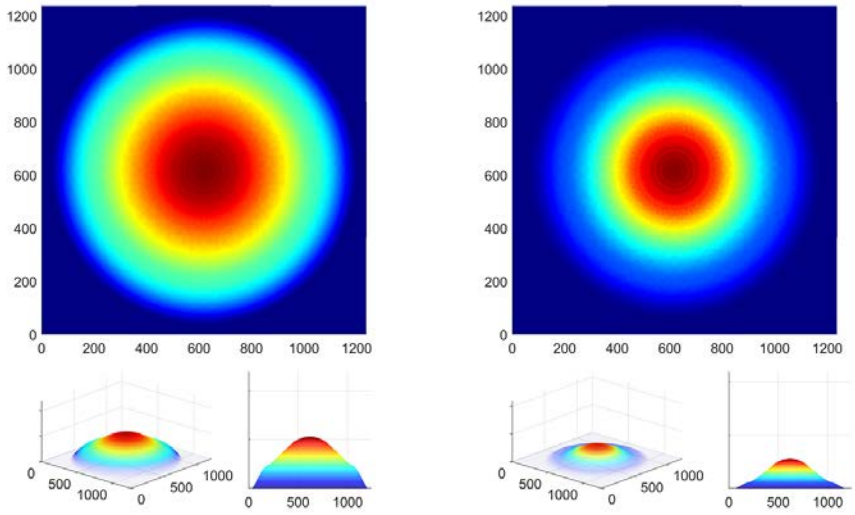

*Fig. 41. Strength E (on the left) and intensity I (on the right) at level 200h (6.4*10^{-3} m)*

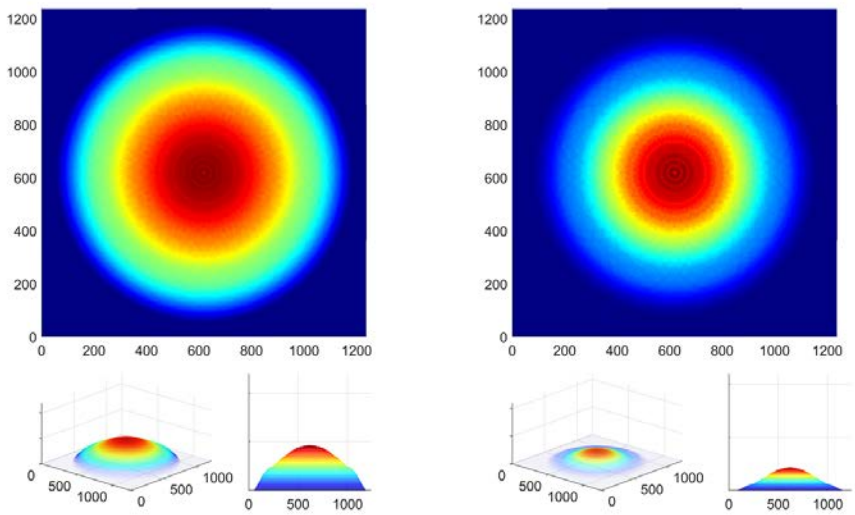

*Fig. 42. Strength E (on the left) and intensity I (on the right) at level 240h (7.68*10^{-3} m)*

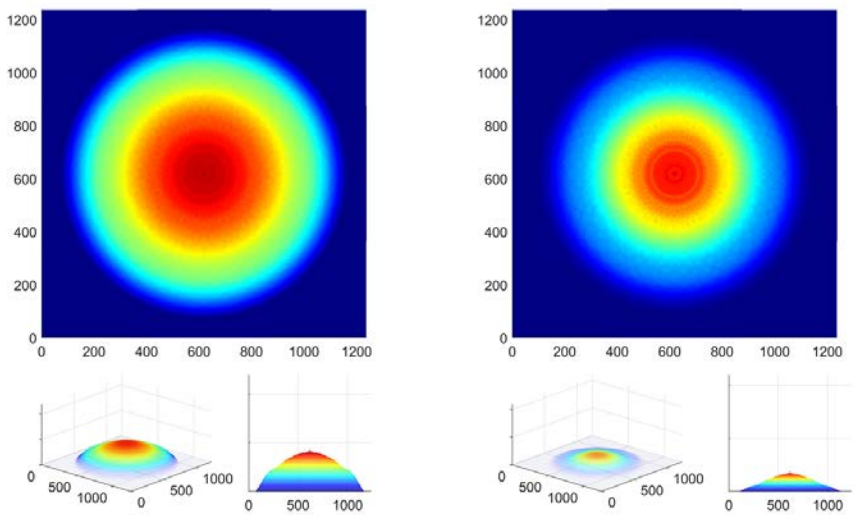

*Fig. 43. Strength E (on the left) and intensity I (on the right) at level 280h (8.96*10^{-3} m)*

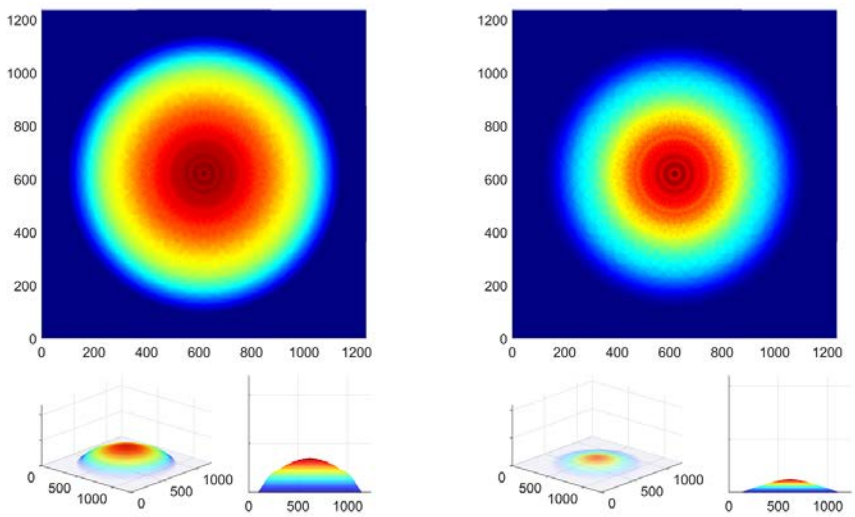

*Fig. 44. Strength E (on the left) and intensity I (on the right) at level 320h (10.24*10^{-3} m)*

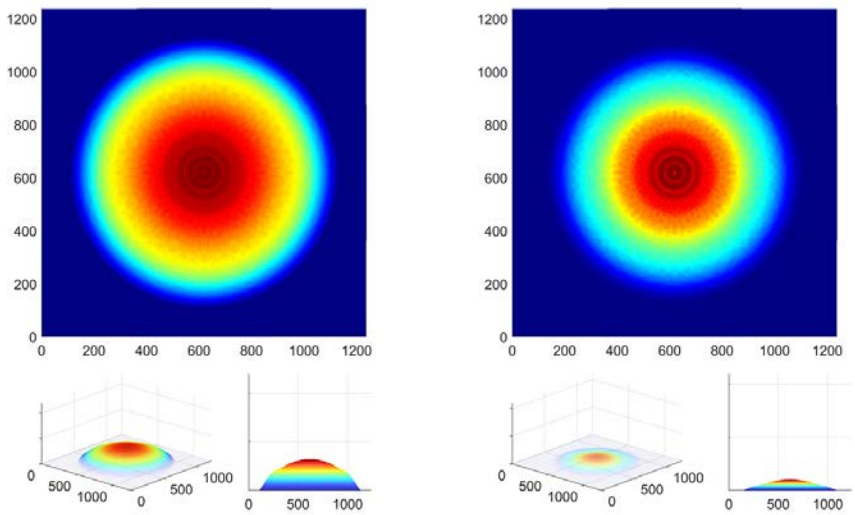

*Fig. 45. Strength E (on the left) and intensity I (on the right) at level 340h (10.88*10^{-3} m)*

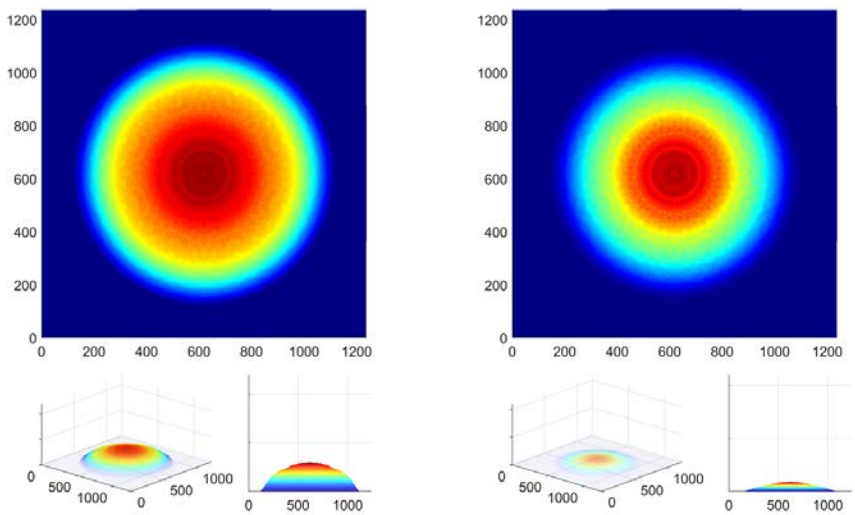

*Fig. 46. Strength E (on the left) and intensity I (on the right) at level 360h (11.52*10^{-3} m)*

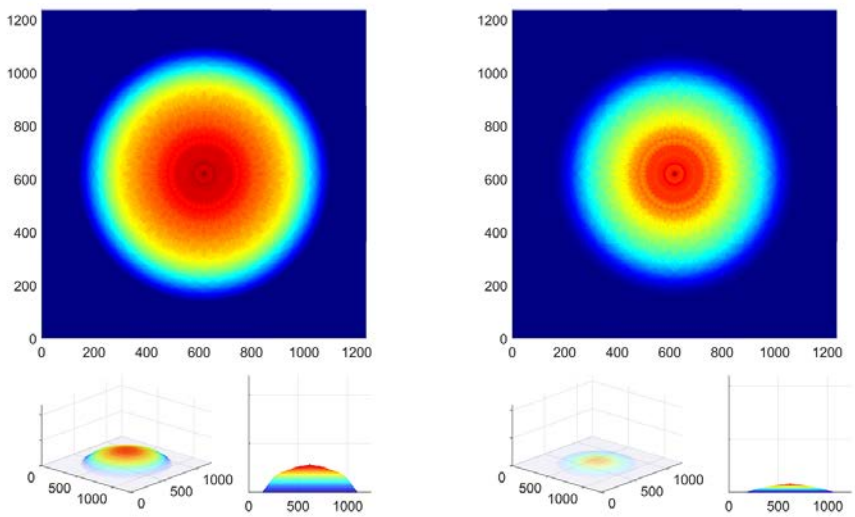

*Fig. 47. Strength E (on the left) and intensity I (on the right) at level 380h (12.16*10^{-3} m)*

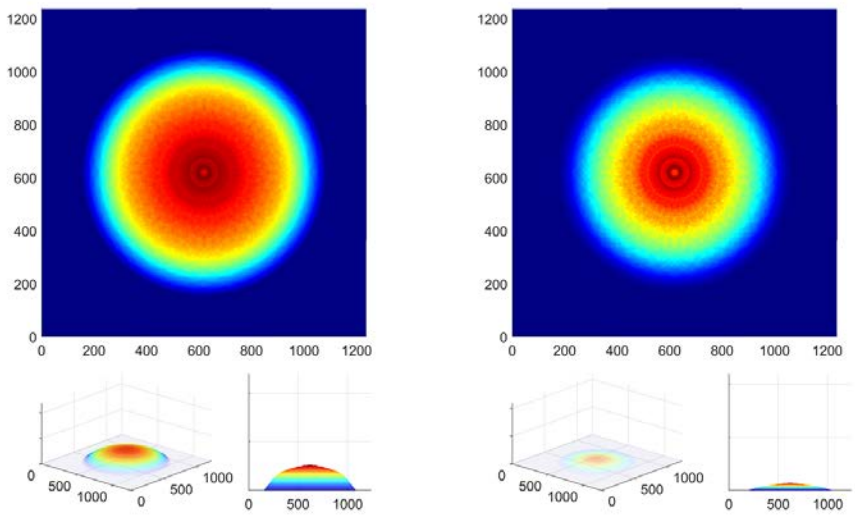

*Fig. 48. Strength E (on the left) and intensity I (on the right) at level 400h (12.8*10^{-3} m)*

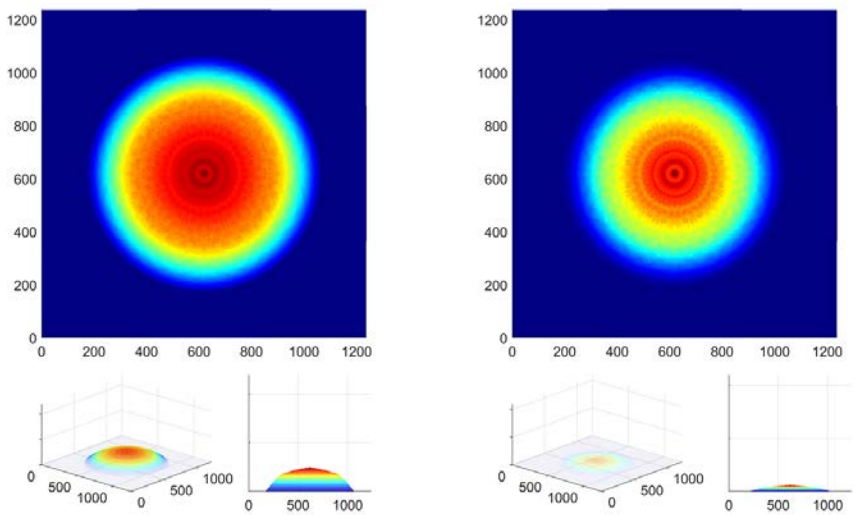

*Fig. 49. Strength E (on the left) and intensity I (on the right) at level 420h (13.44*10^{-3} m)*

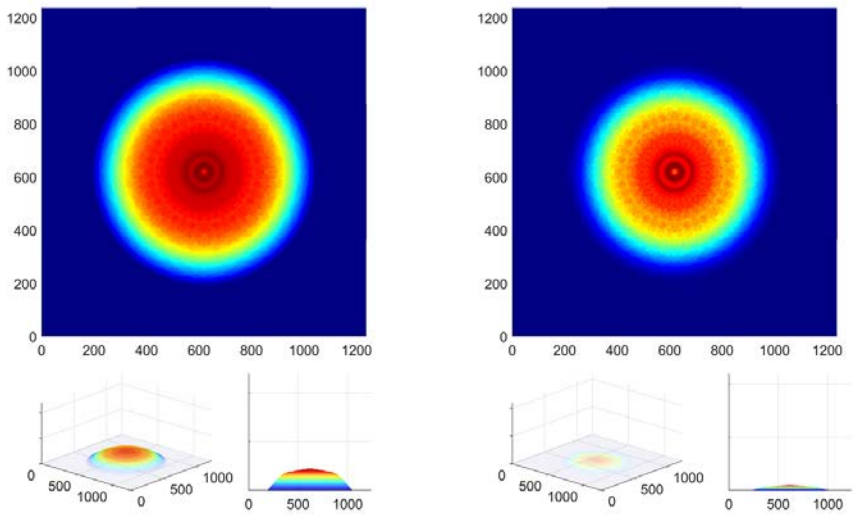

*Fig. 50. Strength E (on the left) and intensity I (on the right) at level 440h (14.08*10^{-3} m)*

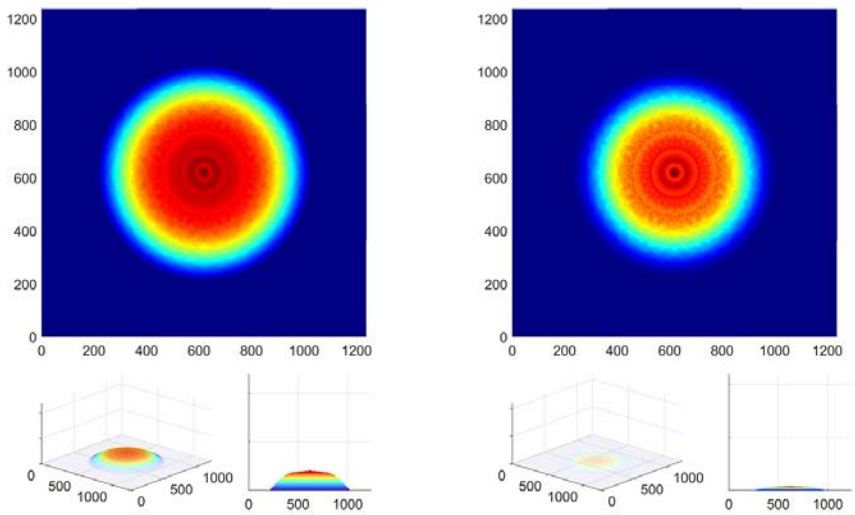

*Fig. 51. Strength E (on the left) and intensity I (on the right) at level 460h (14.72*10^{-3} m)*

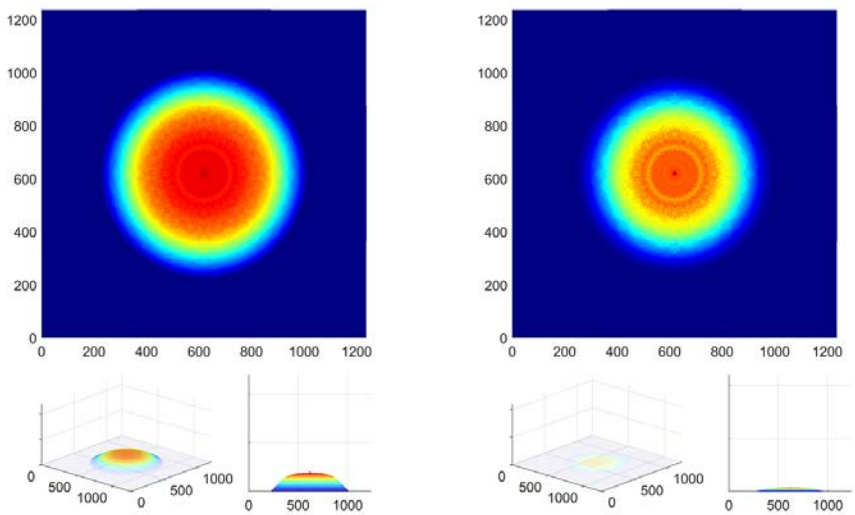

*Fig. 52. Strength E (on the left) and intensity I (on the right) at level 470h (15.04*10^{-3} m)*

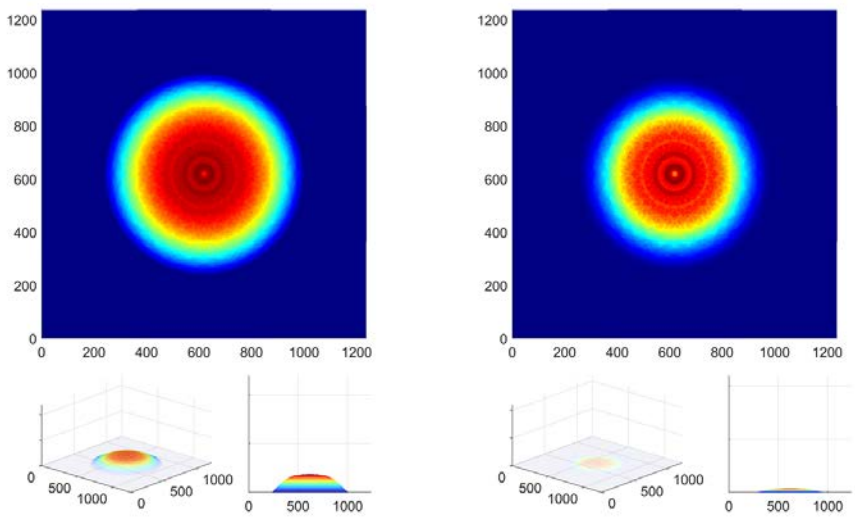

*Fig. 53. Strength E (on the left) and intensity I (on the right) at level 480h (15.36*10^{-3} m)*

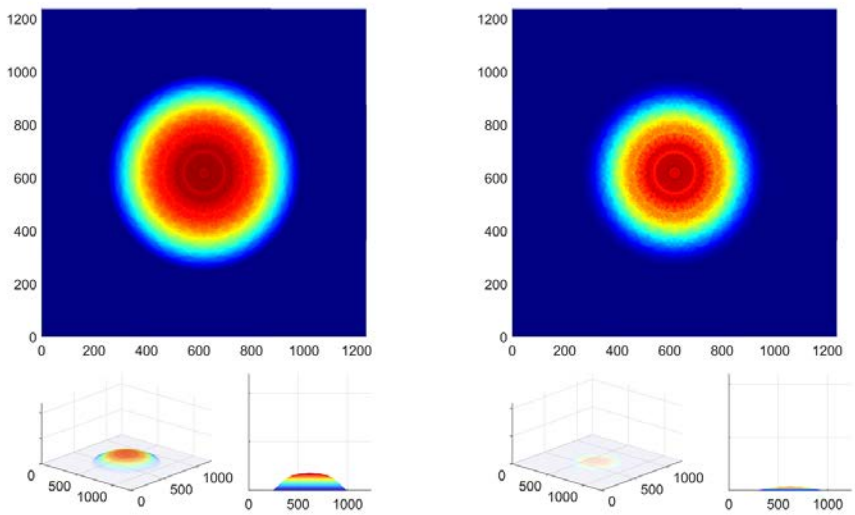

*Fig. 54. Strength E (on the left) and intensity I (on the right) at level 490h (15.68*10^{-3} m)*

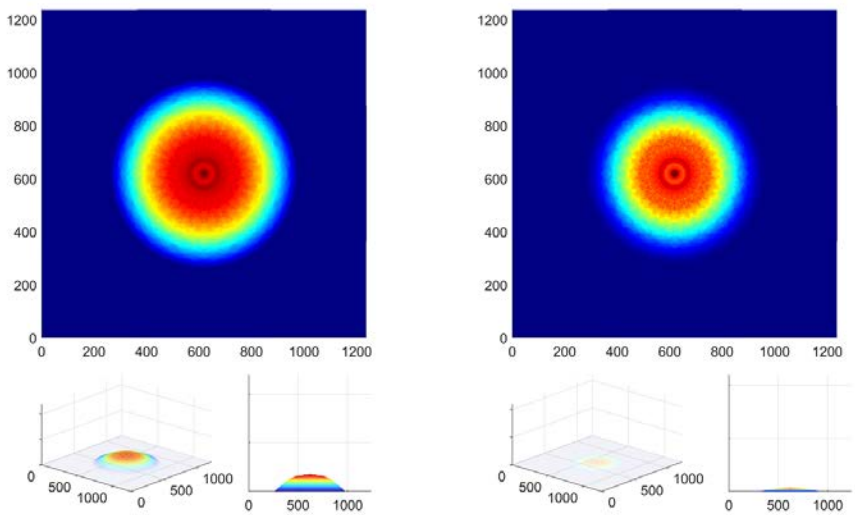

*Fig. 55. Strength E (on the left) and intensity I (on the right) at level 500h (16*10^{-3} m)*

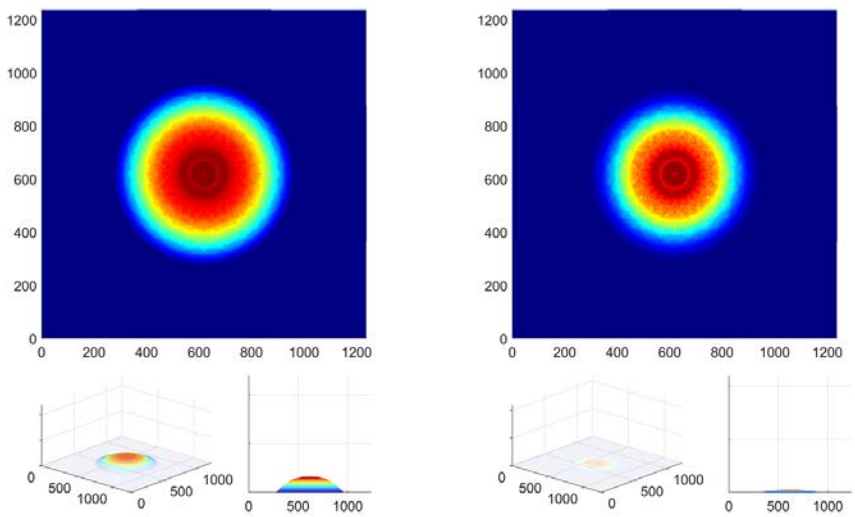

*Fig. 56. Strength E (on the left) and intensity I (on the right) at level 510h (16.32*10^{-3} m)*

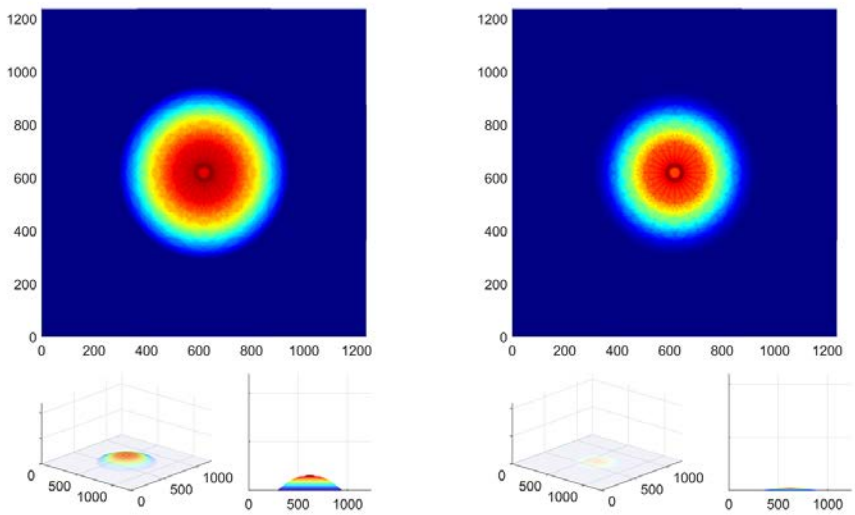

*Fig. 57. Strength E (on the left) and intensity I (on the right) at level 520h (16.64*10^{-3} m)*

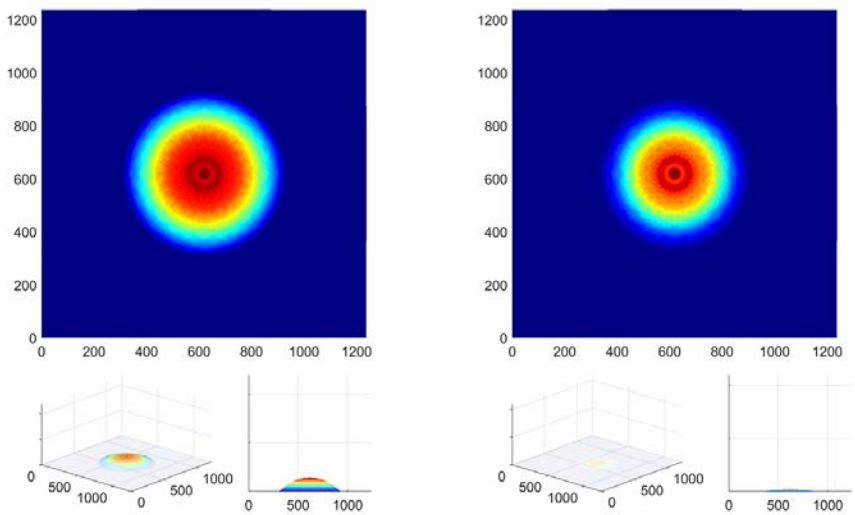

*Fig. 58. Strength E (on the left) and intensity I (on the right) at level 530h (16.96*10^{-3} m)*

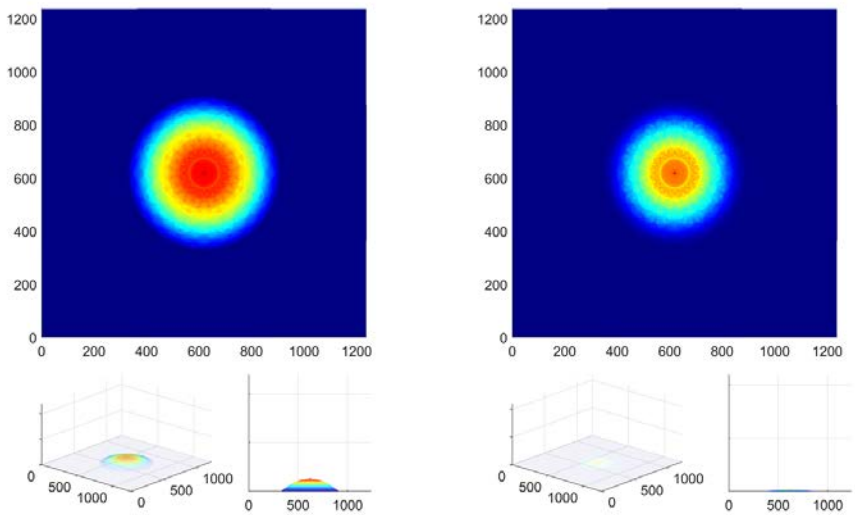

*Fig. 59. Strength E (on the left) and intensity I (on the right) at level 540h (17.28*10^{-3} m)*

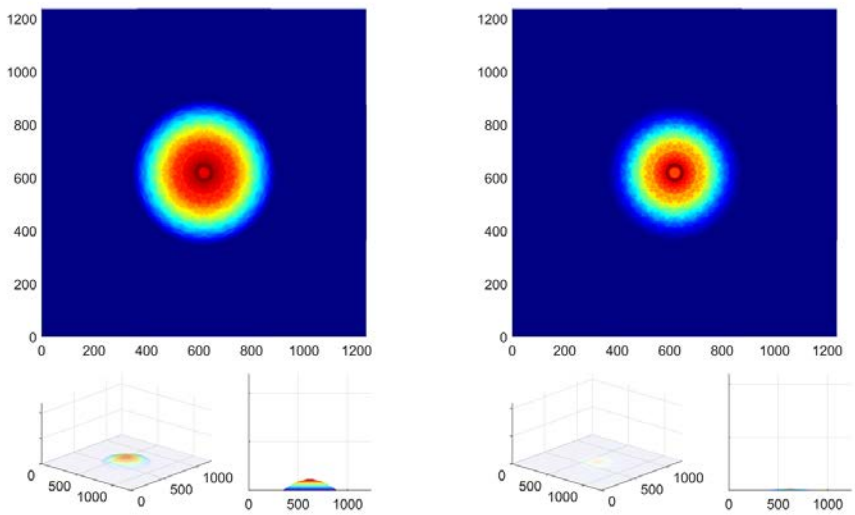

*Fig. 60. Strength E (on the left) and intensity I (on the right) at level 550h (17.6*10^{-3} m)*

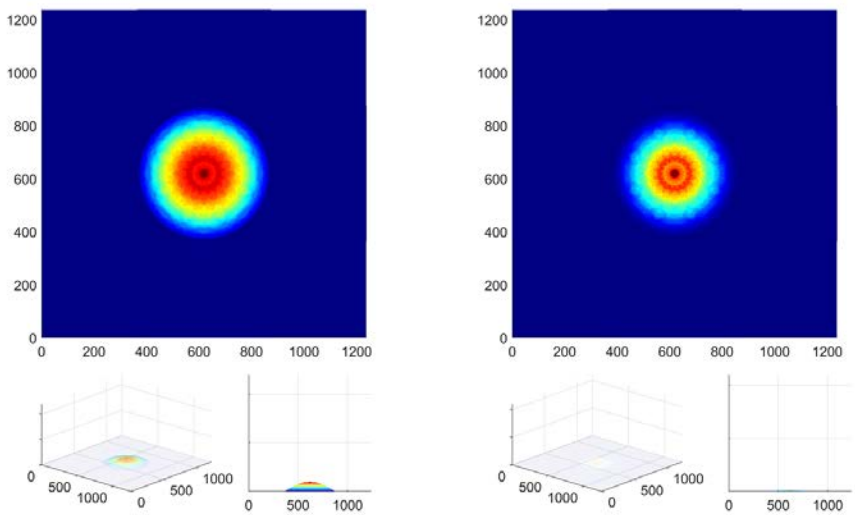

*Fig. 61. Strength E (on the left) and intensity I (on the right) at level 560h (17.92*10^{-3} m)*

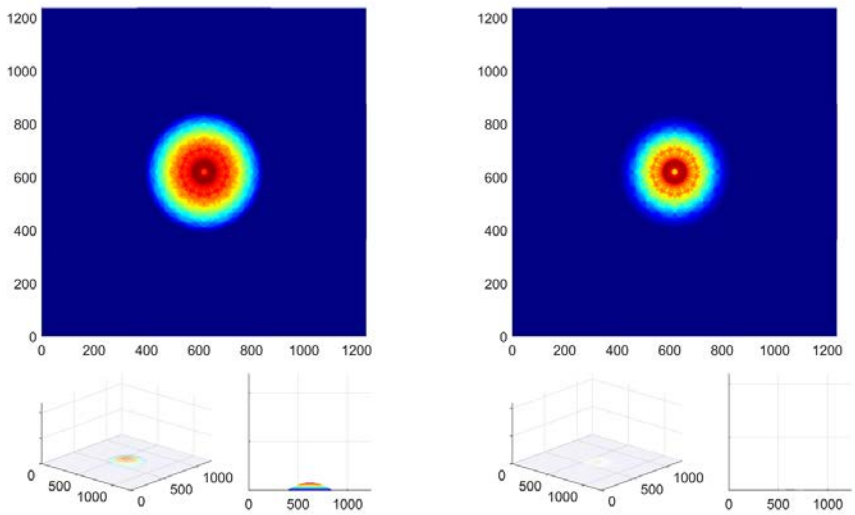

*Fig. 62. Strength E (on the left) and intensity I (on the right) at level 570h (18.24*10^{-3} m)*

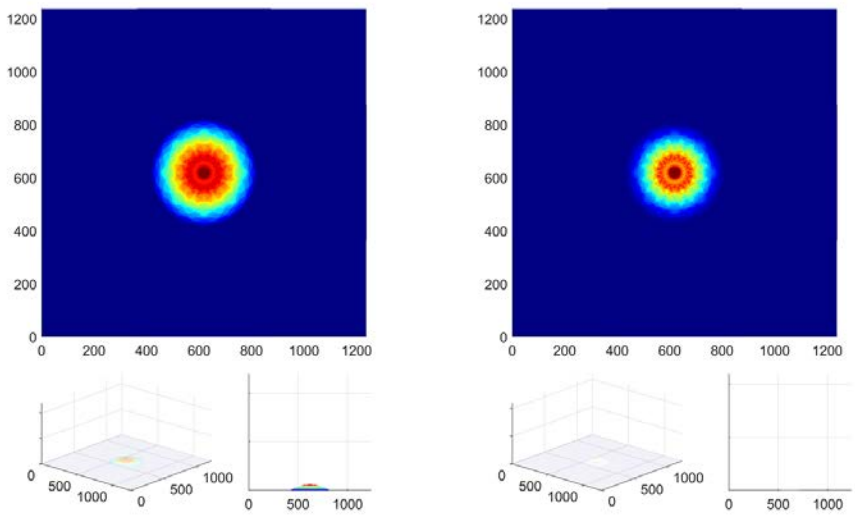

*Fig. 63. Strength E (on the left) and intensity I (on the right) at level 580h (18.56*10^{-3} m)*

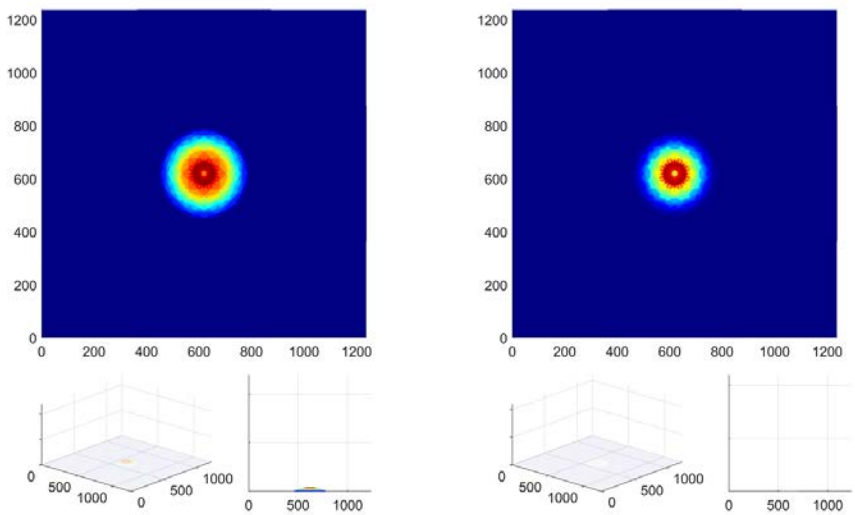

*Fig. 64. Strength E (on the left) and intensity I (on the right) at level 590h (18.88*10^{-3} m)*

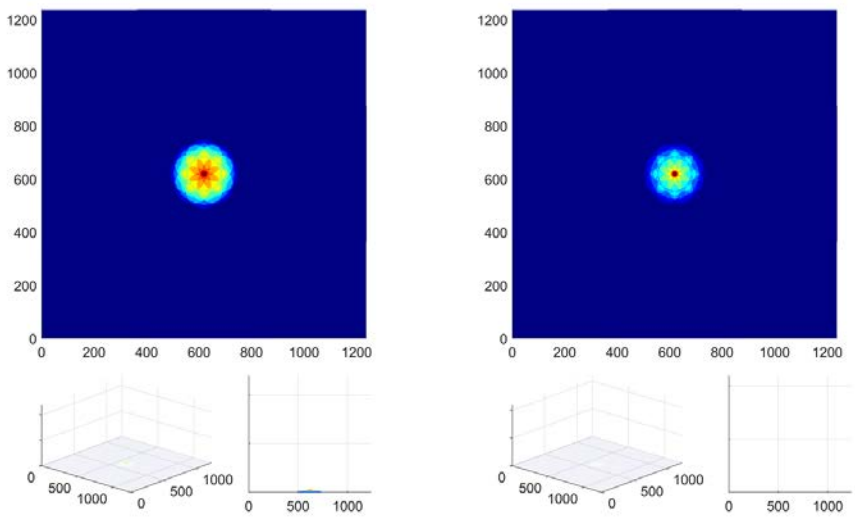

*Fig. 65. Strength E (on the left) and intensity I (on the right) at level 600h (19.2*10^{-3} m)*

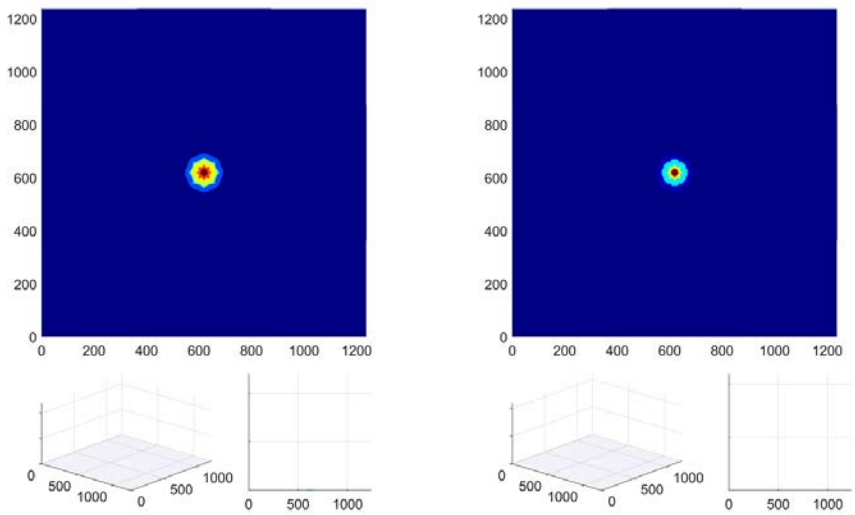

*Fig. 66. Strength E (on the left) and intensity I (on the right) at level 610h (19.5*10^{-3} m)*

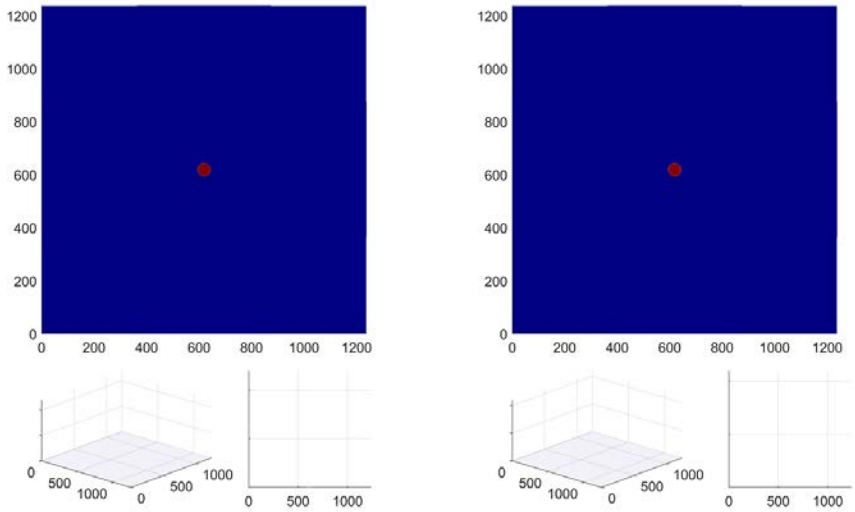

*Fig. 67. Strength E (on the left) and intensity I (on the right) at level 613h (19.616*10^{-3} m)*

When calculating the interaction of the Aires 64P1S5G resonator with incident radiation at 28 GHz, the electric field strength E over the central point of the circuit at height h = 32 μm ($32*10^{-6}$ m) in time with different step Δt was analyzed (Figs 68-92).

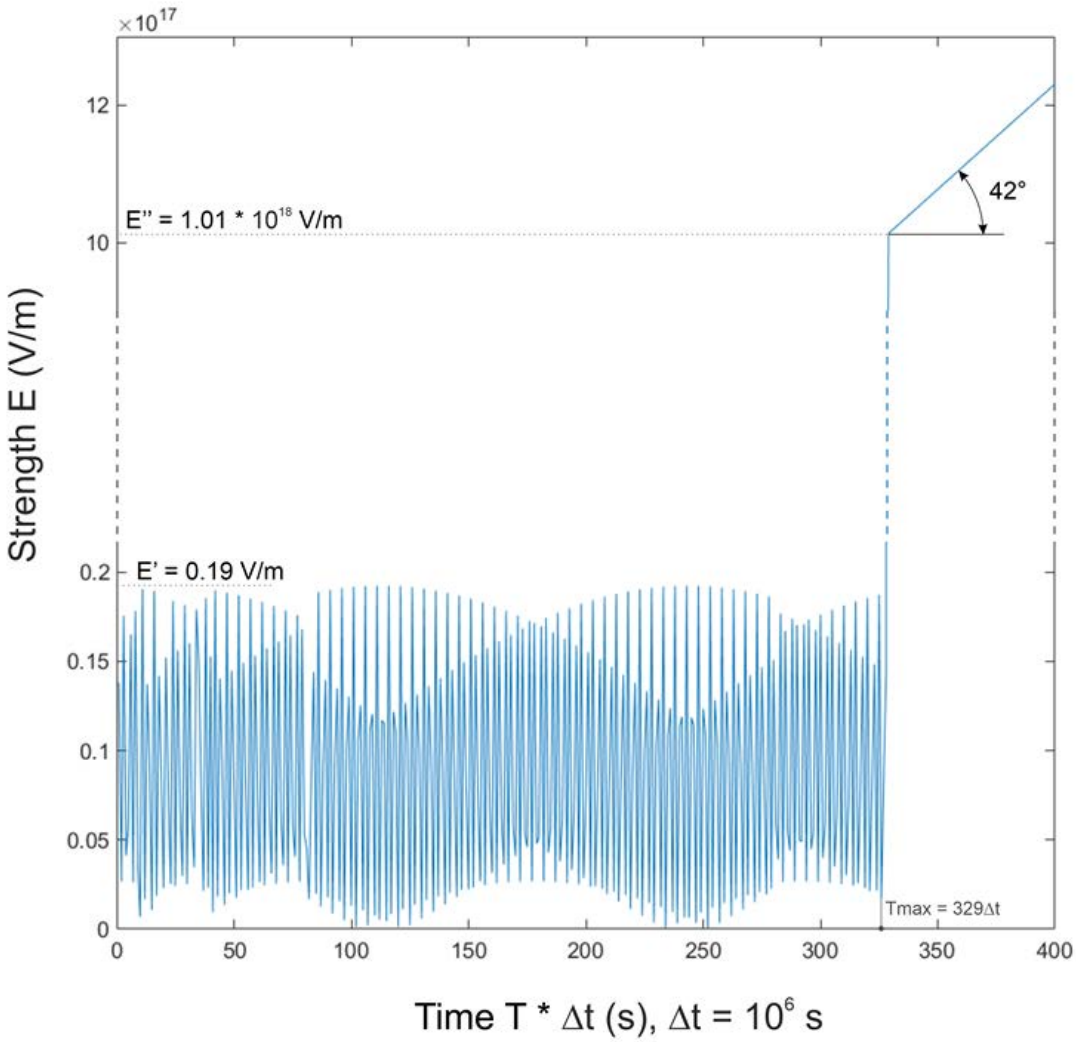

Fig. 68. General graph of the time dependence of the field strength E(T) with step Δt = 10^6 s, the limit at t = 329 Δt c.

Analysis of the graph of the field strength E versus time T over the central point of the Aires 64P1S5G resonator circuit (Fig. 68) showed that after 329 periods Δt the system enters the zone where there is a sharp, one-step jump in potential to $1.01*10^{18}$ (V/m). After that, the potential set begins to go continuously in a straight line at an angle of ~42°. This corresponds to the transformation of the entire system into quantum form. It should also be noted that a regular internal rhythm of subwave categories is present throughout the process.

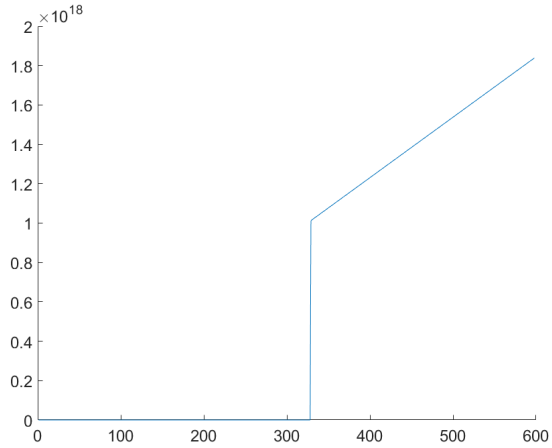

Fig. 69. Graph of field strength over time E(T), Δt =10^6c.

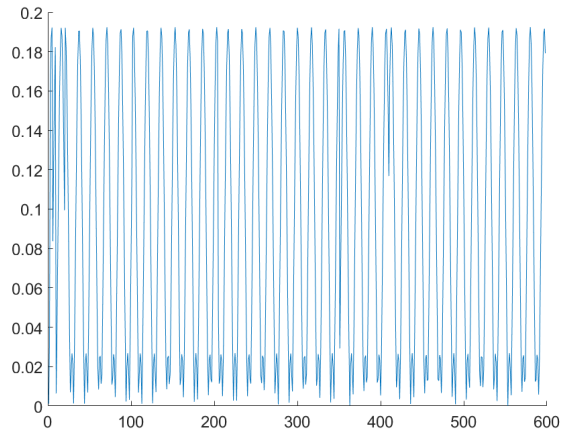

Fig. 70. Graph of field strength over time E(T), Δt =10^5c.

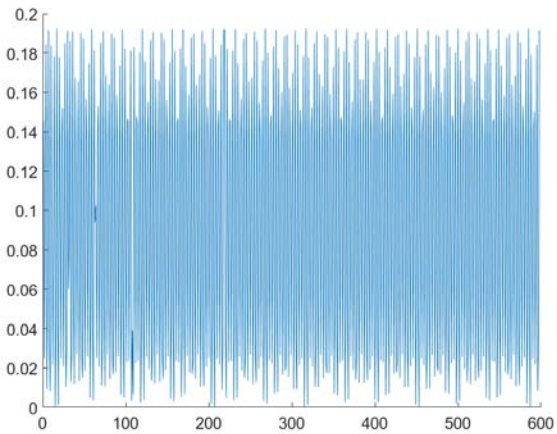

Fig. 71. Graph of field strength over time E(T), Δt =10^4c.

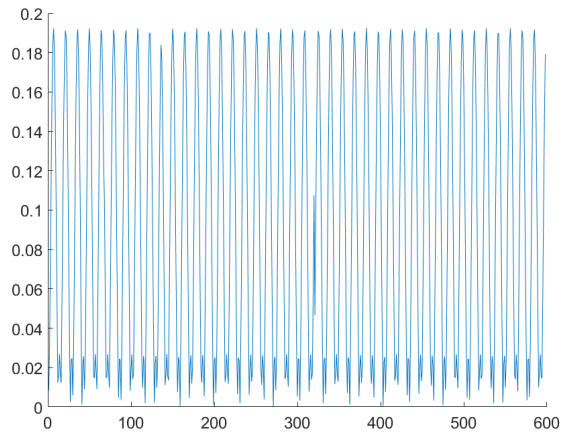

Fig. 72. Graph of field strength over time E(T), Δt =10^3c.

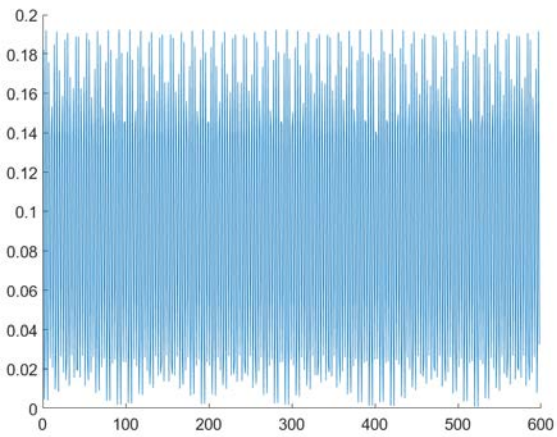

Fig. 73. Graph of field strength over time E(T), Δt =10^2c.

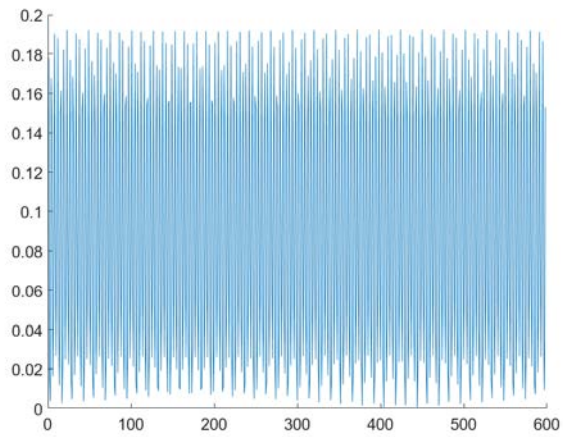

Fig. 74. Graph of field strength over time E(T), Δt =10c.

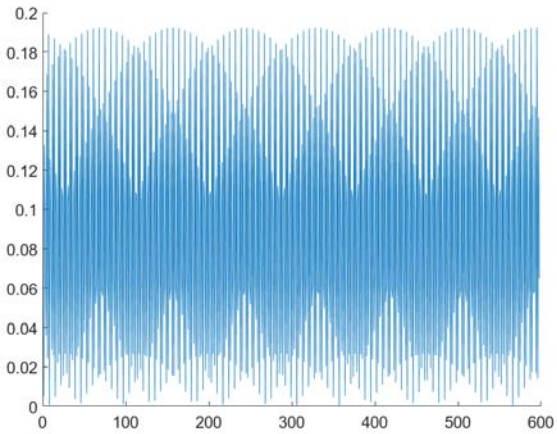

Fig. 75. Graph of field strength over time E(T), Δt =1c.

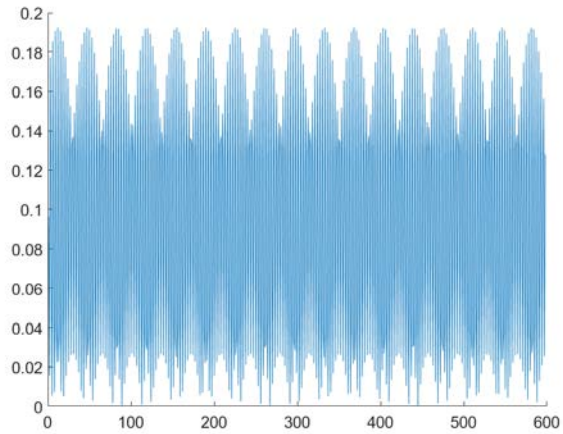

Fig. 76. Graph of field strength over time E(T), Δt =0.1c.

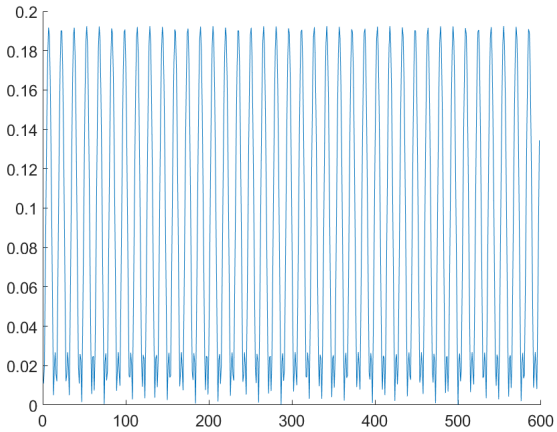

Fig. 77. Graph of field strength over time E(T), Δt =10^{-2}c.

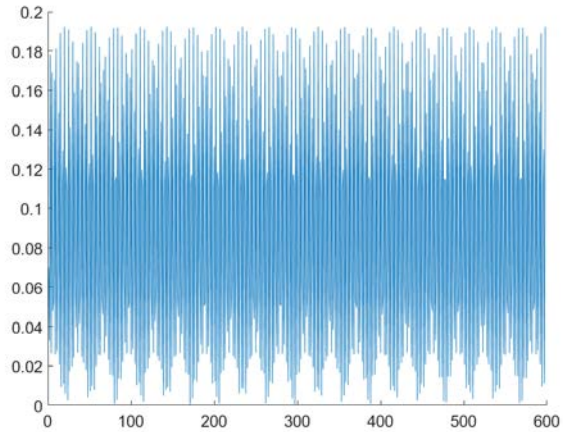

Fig. 78. Graph of field strength over time E(T), Δt =10^{-3}c.

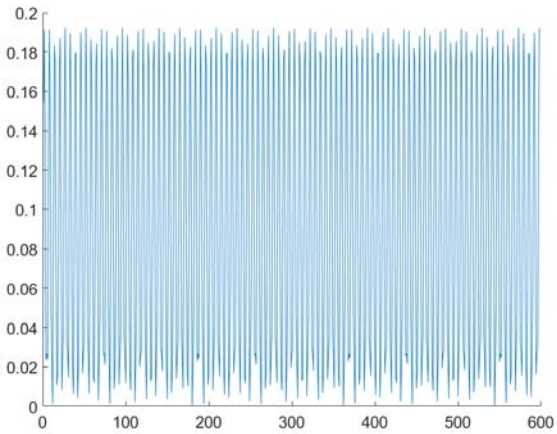

Fig. 79. Graph of field strength over time E(T), Δt =10^{-4}c.

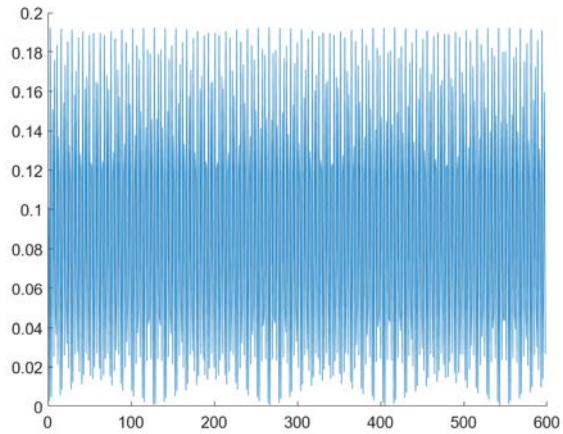

Fig. 80. Graph of field strength over time E(T), Δt =10^{-5}c.

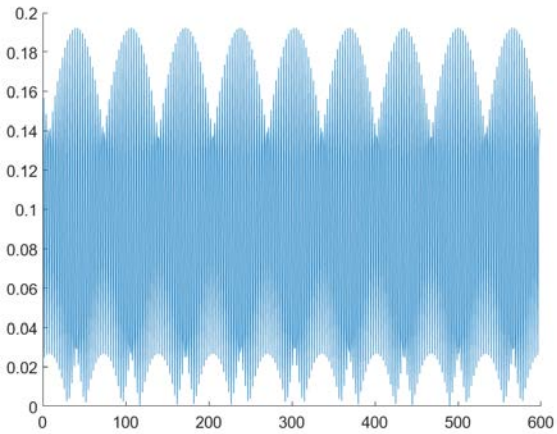

Fig. 81. Graph of field strength over time E(T), Δt =10^{-6}c.

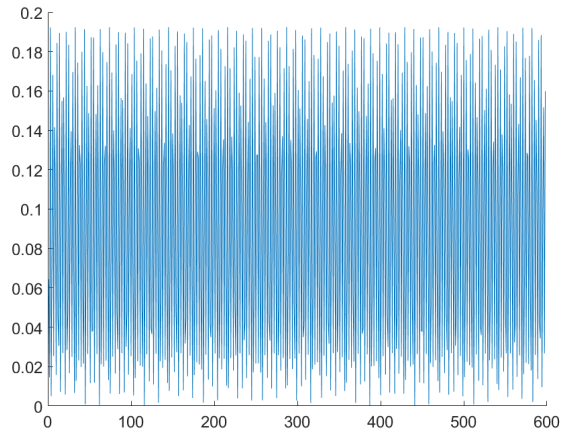

Fig. 82. Graph of field strength over time E(T), Δt =10^{-7}c.

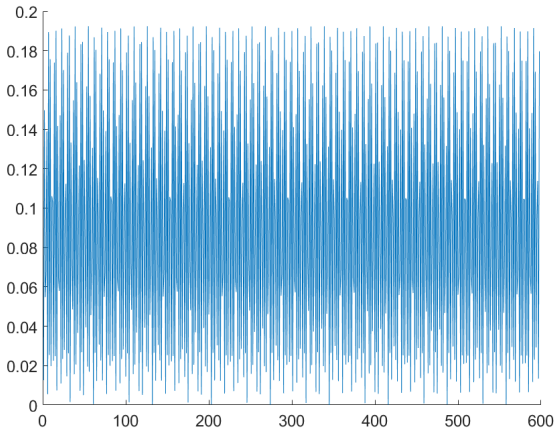

Fig. 83. Graph of field strength over time E(T), Δt =10^{-8}c.

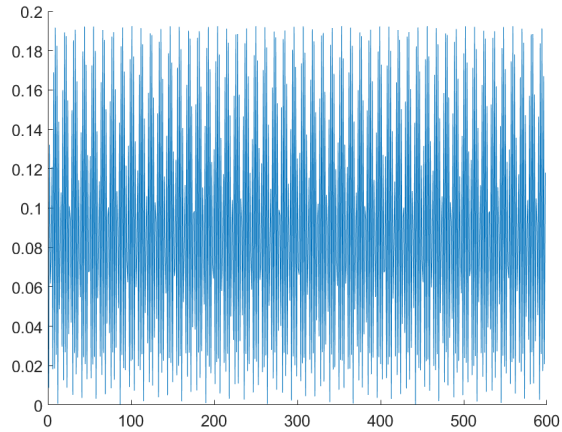

Fig. 84. Graph of field strength over time E(T), Δt =10^{-9}c.

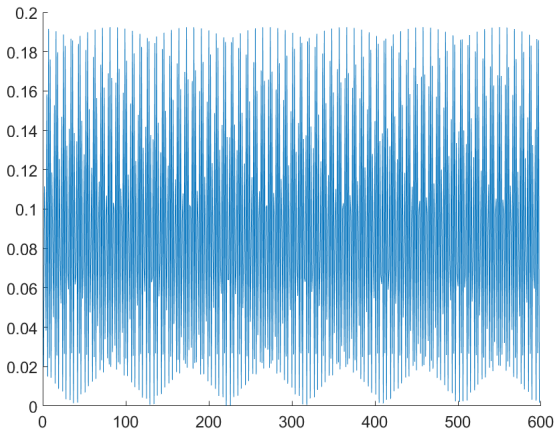

Fig. 85. Graph of field strength over time E(T), Δt =10^{-10}c.

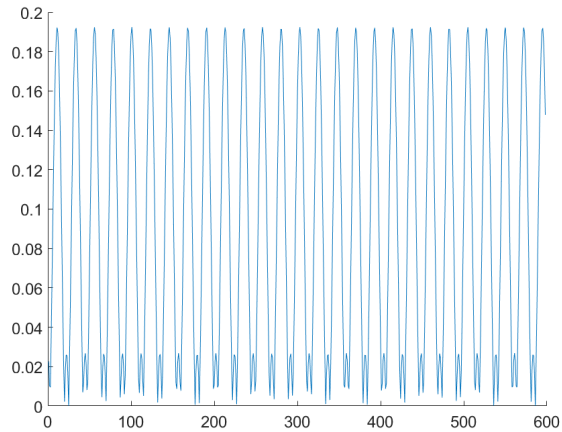

Fig. 86. Graph of field strength over time E(T), Δt =10^{-11}c.

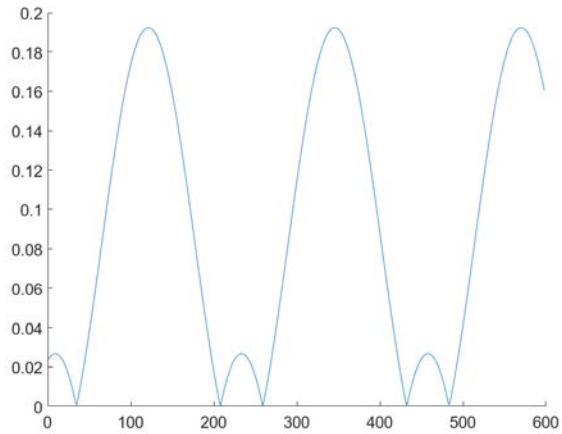

Fig. 87. Graph of field strength over time E(T), $\Delta t = 10^{-12}c$, frequency ν_1 = 2.9 GHz, frequency ν_2 = 9.8 GHz.

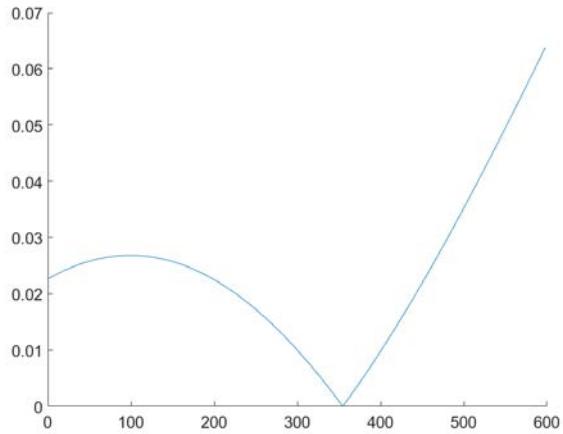

Fig. 88. Graph of field strength over time E(T), $\Delta t = 10^{-13}c$.

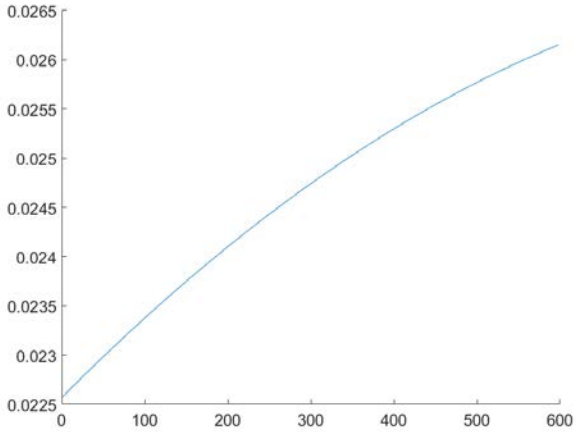

Fig. 89. Graph of field strength over time E(T), $\Delta t = 10^{-14}c$.

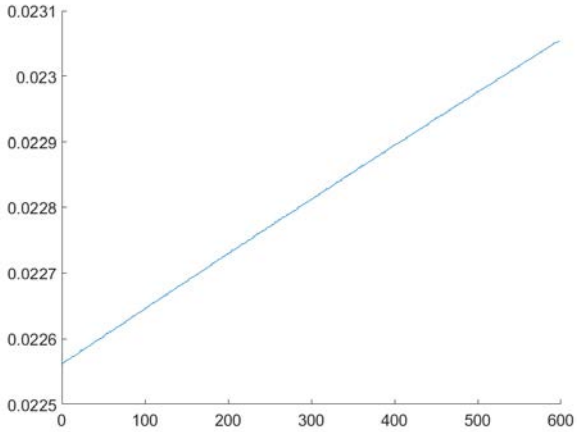

Fig. 90. Graph of field strength over time E(T), $\Delta t = 10^{-15}c$.

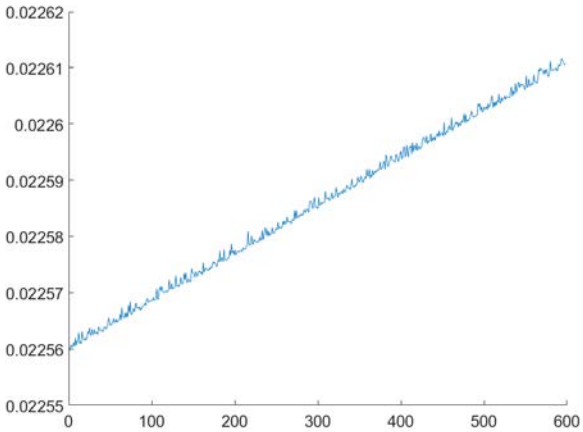

Fig. 91 Graph of field strength over time E(T), $\Delta t = 10^{-16}c$.

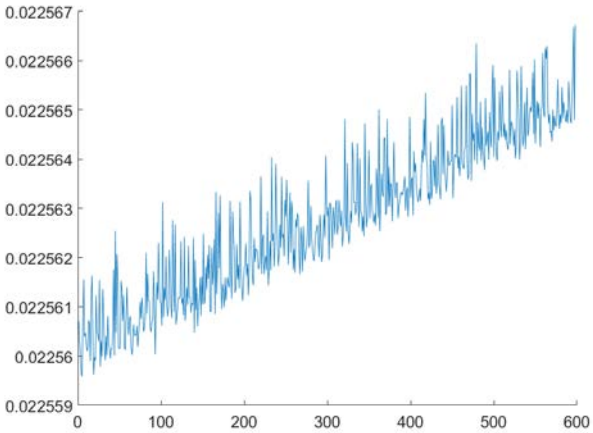

Fig. 92. Graph of field strength over time E(T), $\Delta t = 10^{-17}c$.

As can be seen from the presented images (Figs. 69-92), the regularity of the wave response is preserved throughout the entire time range of studies from 10^6s to 10^{-15}s. With a further decrease in the temporal discrete, the regularity is violated.

When calculating the electromagnetic field strength as a function of time E(T) in steps $\Delta t = 10^{-12}$ s (Fig. 87), a basic two-wave interaction pattern was obtained with frequency $\nu_1 = 2.9$ GHz and amplitude of intensity $E_1 = 0.19$ V/m, and frequency $\nu_2 = 9.8$ GHz and amplitude of intensity $E_2 = 26.8*10^{-3}$ V/m, which is then projected into other frequency ranges.

Undoubtedly, this phenomenon associated with the discrete of system requires additional studies. However, it can be noted that the superposition arising from the Aires 64P1S5G resonator in the form of a stationary field response has a regular character.

The silicon substrate of the Aires resonator (microprocessor) initially has its own electromagnetic superposition, determined by its crystal lattice (n-type monocrystalline silicon substrate with crystallographic plane 100 (Miller index)).

The slit topological pattern formed on the wafer when interacting with incident electromagnetic radiation creates a resonant response over the surface of the resonator in the form of a highly coherent fractal field that interacts with the inherent superposition of the crystal lattice of the silicon substrate, reorganizing the topology of its structural framework according to its own parameters. Thus, based on feedback in the crystal lattice of the substrate, an analog of a stationary fractal pattern arises from a slit matrix deposited on the surface.

Due to the fact that any electromagnetic superposition, according to classical physics, is capable of using feedback to correct the structural organization of the object that initially generates it, we can conjecture with highly probability that a restructuring of the silicon wafer structure, on which the 64P1S5G topological slit pattern is applied, is inevitable, and at a certain stage its structural analogue forms with the formation of reference resonators in the form of matching p-n junctions within this pattern, which, apparently, is specifically linked with the point of modification of the object into quantum form. This hypothesis requires additional X-ray structural studies.

Since the parameter of the unit cell of the crystal silicon lattice is ~ 5.4 Å (Fig. 93), the accuracy of the characteristics of the corrected superposition of the pattern increases by orders of magnitude.

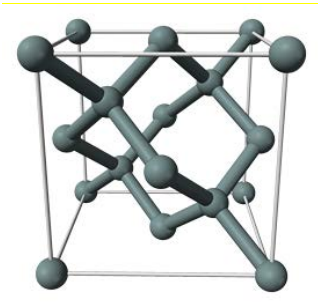

Fig. 93. Silicon crystal lattice

As a result, the wave superposition arising from the modified crystal silicon lattice will be analogous to the fractal pattern formed from the topological slit matrix, which will shift the interaction to the superhigh-frequency range with a corresponding increase in field energy.

According to research conducted at Vilnius University [1], the minimum power of the radiation incident on a wafer must be 2 W to activate a resonant response.

As can be seen from the general graph (Fig. 68), over a period of time $t = 329\Delta t = 329 * 10^6$ s (~10.4 years), the system reaches the limit and transitions to quantum form, which is accompanied by a sharp collection of potential (vertical line) and then, as shown in the graph (straight line at an angle of ~ 42°), a subsequent collection of potential leads to further structural self-development of the pattern, i.e. the process becomes completely correlated, since it does not have cyclic modulations. This suggests that the interaction is harmonized, i.e. the collection of potential and the structural modification take place simultaneously – it's a single process.

It should be taken into account that the circuit was calculated for a frequency of 28 GHz and the corresponding power, which is only one fragment of the huge number of wave fronts of different frequency ranges, which are in the medium and interact with the circuit.

In previous studies on the interaction of a simplified analogue of the pattern with frequencies of 2.4 GHz and 5.5 THz [2-6], the corresponding resonance response was also obtained. In addition, the appearance of a hologram over the pattern (Fig. 94) suggests that the resonator's

pattern creates the corresponding structural response in the optical frequency range.

Based on the foregoing, it can be argued that when the 64P1S5G pattern interacts with broadband electromagnetic radiation of various frequencies in real conditions, including very high frequencies carrying the corresponding potential, and power, its transition to a quantum form can occur extremely quickly, even simultaneously, after the initial activation of the pattern, which opens up very broad possibilities for the use of this effect in various fields of application.

In summary, given external irradiation of the Aires microprocessor, the resonance response is an integral, stationary, highly coherent, symmetric, self-affine superposition from the interaction of surface waves with annular slits, concentrating the electric potential in them, thus causing them to begin working as waveguides. The points where the rings intersect initiate the phase matching of counter flows, thereby triggering the appearance of a stationary (standing) wave, which is clearly seen in the computer simulation. As a result, the emerging reflex represents a whole complex of corresponding, inter-integrated, fractal (self-similar) interactions.

The animation (Appendix 3) shows the consecutive responses of the Aires resonator (microprocessor) to the influence of electromagnetic radiation in different sections from the edge of the resonator to its center in the form of a distribution of the strength and energy flux density of the electromagnetic field.

CONCLUSION

The simulations showed that given electromagnetic action at a frequency of 28 GHz on an Aires 64P1S5G self-affine resonator (microprocessor), the device converts incident electromagnetic radiation into a coherent spatio-temporal self-affine form (hologram). In particular, over the central region of the resonator, there is a marked increase in both the strength E_{max} = 3.44*10^3 (V/m) (~ in 1.5*10^6 times) and the intensity of the electromagnetic field I_{max} = 1.18*10^7 (W/m^2) (~ in 2.23*10^{12} times).

Further, within the ring of maximum response intensity, a counter resonance forms along its diameters, causing the values of the potentials participating in this process to be multiplied. As a result of counter-harmonization with respect to amplitudes, frequencies, phases, and the radiation pattern, there is a maximally neutral zone in the center and, since an active potential always redistributes from zones of maximum amplitude activity to a neutral zone, the potential density at the central point increases sharply, and the amplitude tends to zero, which initiates the singularity phenomenon. According to the first law of thermodynamics (the law of conservation of energy), energy doesn't appear out of nowhere or vanish into nothing – rather it transforms from one state into another, which is what happens in the central point of the circuit as the point of singularity. As a result, the focal point of the vector interaction of all processes with a common potential arises at the center of the circuit:

$$(I_{max})^2 = (1.18*10^7)^2 = 1.39*10^{14}\ (W/m^2).$$

In addition, the constant inflow of potential from the outside, which strives to fill the circuit's neutral zone, ensures that the emerging superposition is highly stable.

This state of the system is a consequence of the fundamental symmetry principle underlying the fractal topology of the Aires resonators, which is formulated in Noether's theorem, which states that a certain conservation law corresponds to each continuous symmetry of a physical system.

$$\sum_{i=1}^{n} \frac{\partial \mathrm{L}}{\partial \dot{\mathrm{x}}_i} \delta_i = constant \qquad (2),$$

where L is the Lagrangian, functions δ_i are random variations.

The theorem can also be formulated the other way around: conservation laws are a consequence of fundamental symmetry. Thus, the arising stationary wave superposition is a manifestation of fundamental physical laws based on the principle of multilevel symmetry. As a consequence, the stability of the wave pattern, and hence the capacity to accumulate and fix the potential within such a system, goes to a fundamentally different level.

Thus, the energy of radiation coming from a Wi-Fi source (router) and modern mobile communication equipment (smartphone, telephone, etc.), after interaction with the resonator, is redistributed in space and across frequencies, phases, and the interaction diagram, transforming into a self-affine stationary structure (hologram) corresponding to the self-affine topological lattice of a resonator carrying analogous properties (coherent transformation).

The field (electromagnetic superposition) (Fig. 94) that results from the Aires 64P1S5G resonator's (microprocessor's) interaction with incident radiation (28 GHz) is self-affine, possess traits of holograms, and, according to the Gabor-Denisyuk theory of holograms, which states that any hologram bears all the same traits as the agent initiating the hologram, becomes a coherent transformer of any waves that interact with it in the corresponding frequency range.

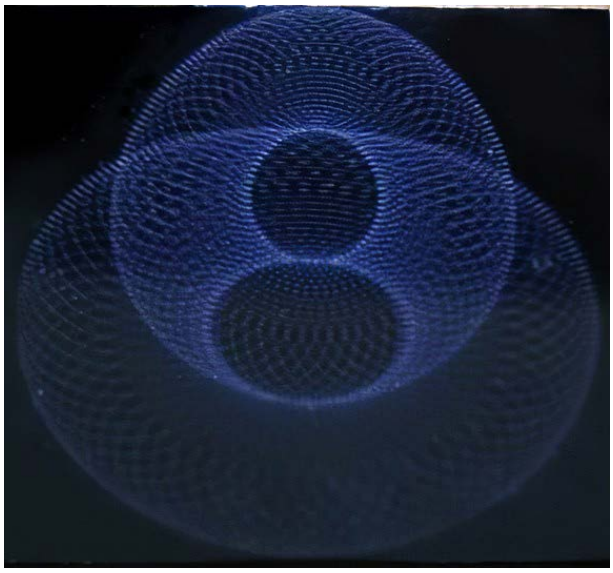

Fig. 94. Natural photo of the hologram on the Aires 64P1S5G microprocessor.

The results of the simulation demonstrate the redistribution of the characteristics of the electromagnetic field (strength and energy flux density), which reach their maximum values in the central part of the circuit, with a sharp condensation of the matched potential at its central point, which makes it possible to speak of the resulting stationary, spatial-wave electromagnetic reflex's ability to direct transform into a highly coherent form the

electromagnetic radiation that interacts with it if that potential does not exceed the potential of the emerging reflex.

Based on the foregoing, we can state that the AIRES 64P1S5G microprocessor used in the LIFETUNE Room and LIFETUNE Personal (2020 model) is a space-time amplitude-frequency converter (Fourier filter) that converts a dynamic wave pattern (28 GHz) into a stationary electromagnetic field that harmonizes external incident radiation in terms of amplitudes, frequencies, phases and the interaction diagrams and, thus, is a catalyst for coherent transformation of electromagnetic radiation interacting with it in the corresponding range of amplitudes and frequencies.

Consequently, in the presence of Aires 64P1S5G resonator (microprocessor), the effect of harmonizing the external man-made radiation (28 GHz) with a biological organism's inherent radiation will be clearly expressed, which is confirmed by numerous tests with living objects, including the human body.

BIBLIOGRAPHY

1. A. Jukna Studies of the prototype of the converter-resonator of electromagnetic radiation, Stage report, Vilnius, 2016.
2. I.N. Serov, A.V. Kopyltsov, K.A. Korshunov, I.A. Soltovskaya, G.N. Lukyanov Calculation of electric field strength given background electromagnetic radiation's interaction with the AIRES C8 resonator (microprocessor), 2017.
3. I. Serov, K. Korshunov, I. Soltovskaya, T. Shamko R&D: Calculation of the strength and intensity of the electromagnetic field in the interaction of electromagnetic radiation at a frequency of 2.4 GHz (Wi-Fi) with an Aires K8 resonator (microprocessor), which is used in the Aires Shield Extreme (2016 model), 2018.
4. I. Serov, K. Korshunov, I. Soltovskaya, T. Shamko, A.V. Kopyltsov, A. Jukna R&D: Calculation of the strength and intensity of the electromagnetic field in the interaction of electromagnetic radiation at a frequency of 2.4 GHz (Wi-Fi) with an Aires C16S resonator (microprocessor), which is used in the Aires Shield Pro (2018 model), 2018.
5. I. Serov, K. Korshunov, I. Soltovskaya, T. Shamko, A.V. Kopyltsov, A. Jukna R&D: Calculation of the strength and intensity of the electromagnetic field in the interaction of electromagnetic radiation at a frequency of 2.4 GHz (Wi-Fi) with an Aires C28S resonator (microprocessor), which is used in the Aires Defender Pro (2018 model), 2018.
6. I. Serov, K. Korshunov, I. Soltovskaya, T. Shamko, A.V. Kopyltsov, A. Jukna R&D: Calculation of the strength and intensity of the electromagnetic field in the interaction of electromagnetic radiation at a frequency of 2.4 GHz (Wi-Fi) with an Aires C32S resonator (microprocessor), which is used in the Aires Guardian (2018 model), 2018.
7. I. Serov, K. Korshunov, I. Soltovskaya, T. Shamko, A.V. Kopyltsov, A. Jukna R&D: Calculation of the strength and intensity of the electromagnetic field in the interaction of electromagnetic radiation at a frequency of 6 GHz (Wi-Fi 5G) with an Aires C20S5G resonator (microprocessor), which is used in the Aires Crystal (2019 model), 2018.
8. I. Serov, K. Korshunov, I. Soltovskaya, T. Shamko, A.V. Kopyltsov, A. Jukna R&D: Calculation of the strength and intensity of the electromagnetic field in the interaction of electromagnetic radiation at a frequency of 28 GHz (Wi-Fi 5G) with an Aires C20S5G resonator (microprocessor), which is used in the Aires Crystal (2019 model), 2018.
9. Kopyltsov A., Lukyanov G., Serov I. Coherent emission of Electromagnetic Radiation from the surface of semiconductor plate with the self-affine relief // The 3rd International IEEE Scientific Conference on Physics and Control (PhysCon 2007). September, 3rd-7th, Potsdam, Germany.

Appendix 1

TOPOLOGY OF THE AIRES 64P1S5G RESONATOR (MICROPROCESSOR)

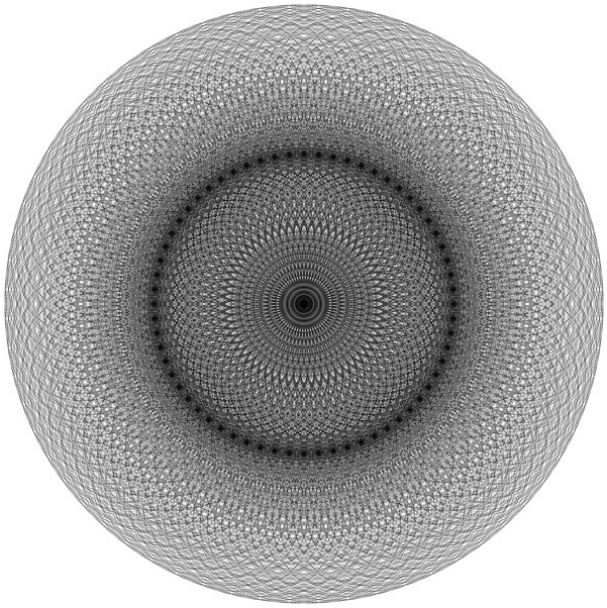

Appendix 2

HARDWARE AND SOFTWARE

Hardware:

- Server: Supermicro CSE-733TQ-665B
- Processor: Intel Xeon E5-2620 v2 2.1 GHz (6-core) x 2.
- RAM: Kingston DDR3-1600 MHz, 256 GB
- Video card: NVIDIA GeForce RTX 2070 SUPER

Software:

- PascalABC.NET v.3.3
- MATHLAB R2015b

Appendix 3

ANIMATION

The dynamics of the computer simulation process can be viewed here: https://yadi.sk/i/8KiYVJ9XaAkuQA .